Chemical Science

ROYAL SOCIETY OF CHEMISTRY

EDGE ARTICLE

View Article Online
View Journal



Cite this: DOI: 10.1039/d6sc00023a

All publication charges for this article have been paid for by the Royal Society of Chemistry



# A protein-based model of carbon monoxide dehydrogenase exhibits tunable covalency across cluster oxidation and ligand-bound states

Luke C. Lewis, [a] Prajakta Badve, [c] Itzel P. Vaca, [b] Pujan Ajmera, [b] Yuri Lee, [b] Anastassia N. Alexandrova, [b] Katlyn K. Meier [c] and Hannah S. Shafaat *[ab]

The nickel-containing carbon monoxide dehydrogenase (CODH) uses a unique heterometallic [$NiFe_4S_4$] cluster active site, called the C-cluster, to catalyze the reversible reduction of carbon dioxide ($CO_2$) to carbon monoxide (CO) at low overpotential and with perfect selectivity. Only the properly assembled nickel-bound form is capable of this reactivity, though how the structure of the cluster promotes such selectivity remains poorly understood. We have developed a model of the C-cluster by constructing a [$NiFe_3S_4$] cluster in the iron–sulfur cluster binding site of the *Pyrococcus furiosus* ferredoxin protein (NiFd) that replicates the thiolate ligation and aqueous environment of the native system. In this work, we interrogate the roles of each individual metal site and the whole-cluster covalency across two oxidation states that mirror the C-cluster in the $C_{ox}$ and $C_{red1}$ states. We have also studied the system bound to a CODH substrate (CO) and C-cluster inhibitor ($CN^-$). A comprehensive suite of spectroscopic techniques, including pulsed electron paramagnetic resonance (EPR), variable-temperature, variable-field Mössbauer, and high-energy resolution fluorescence-detected X-ray absorption (HERFD-XAS) spectroscopy, have been used in conjunction with quantum mechanics/molecular mechanics (QM/MM) and broken symmetry density functional theory (BS-DFT) calculations to elucidate the electronic properties of these heterometallic clusters. This work reveals that the supporting iron-sulfide subcluster and thiolate ligands play a critical role in buffering charge density as the cluster traverses multiple states. An unusually weak exchange interaction between the Ni site and the iron atoms is found to exist in the CO-bound form, suggesting that substrate binding electronically isolates the nickel site, giving a low-spin ground state that drives localized chemistry to occur at the nickel center. These results have implications for understanding how reactivity is controlled in native CODH to promote CO oxidation and $CO_2$ reduction rather than deleterious hydrogen evolution.

Received 2nd January 2026
Accepted 31st March 2026

DOI: 10.1039/d6sc00023a

rsc.li/chemical-science

## Introduction

Iron–sulfur clusters are ubiquitous in nature, performing a wide variety of functions in all kingdoms of life.[1,2] While iron–sulfur clusters are best known for their role in electron transfer, these cofactors also catalyze important chemical transformations in different protein scaffolds, including the diverse range of reactivity associated with the radical *S*-adenosylmethionine enzymes.[1,3–5] A smaller subset of iron–sulfur clusters contain a heterometallic [$MFe_xS_y$] cluster active site and are found in gas cycling and energy converting enzymes such as nitrogenase and carbon monoxide dehydrogenase (CODH).[6–9]

CODH is a homodimeric enzyme found in anaerobic bacteria and archaea that catalyzes the reversible reduction of carbon dioxide ($CO_2$) to carbon monoxide (CO), with perfect selectivity and negligible overpotential under ambient temperatures and pressures.[7,10–12] The active site of CODH contains a unique heterometallic [$NiFe_4S_4$] cluster, known as the C-cluster, which is comprised of a single exogenous Fe site ($Fe_u$) coupled to a cubane [$NiFe_3S_4$] subsite through one bridging sulfide (Fig. 1).[13–15] While there have been extensive efforts put forward to understand the mechanism of $CO_2$ reduction by CODH, only two intermediates have been quantitatively isolated and structurally characterized, and spectroscopic metrics of the active site remain unclear due to the complexity of the native system.[7,16–19] Thus, it has become desirable to develop a model that recreates key structural motifs of the active site in a simplified system to permit comprehensive characterization of the geometric and electronic structure.[6,20–22]

In response to this, we have developed a protein-based model of CODH using a nickel-substituted ferredoxin protein

[a]*Department of Chemistry and Biochemistry, The Ohio State University, Columbus, Ohio 43210, USA*

[b]*Department of Chemistry and Biochemistry, University of California Los Angeles, Los Angeles, California 90095, USA. E-mail: shafaat@ucla.edu*

[c]*Department of Chemistry, University of Miami, Cox Science Center, 1301 Memorial Drive, Coral Gables, Florida 33146, USA. E-mail: kmeier@miami.edu*

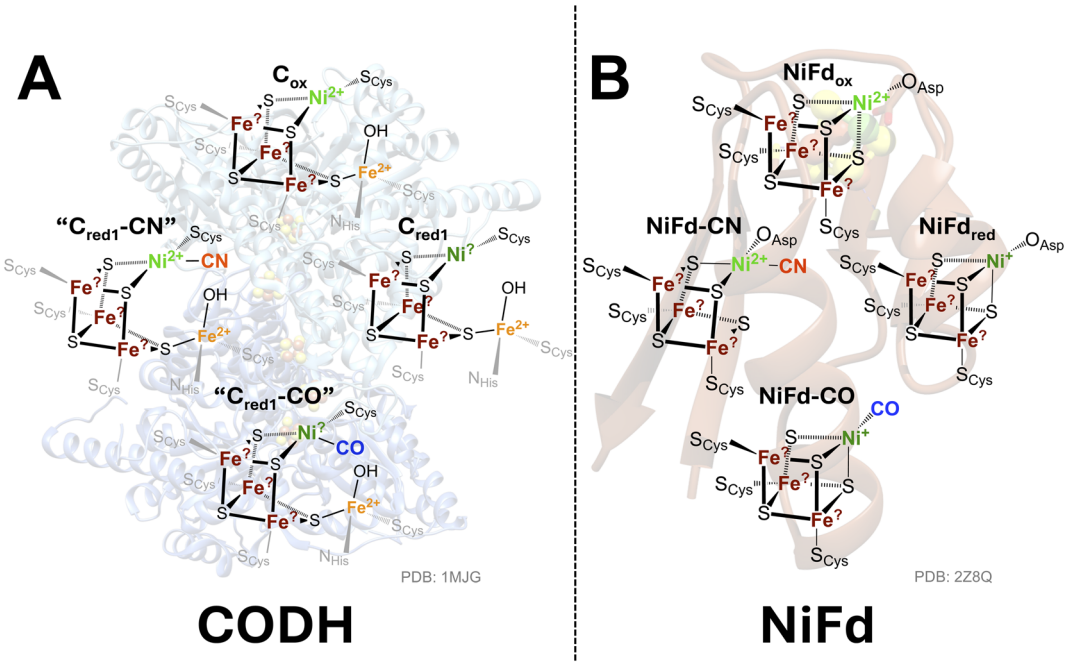


Fig. 1 Geometric structures and proposed oxidation states of (A) key CODH intermediates and the (B) analogous NiFd states.

(NiFd) from *Pyrococcus furiosus*.[23–25] We have shown that this model binds CO, a substrate of CODH, and $CN^-$, an inhibitor of CODH, at the nickel site, offering stable and isolable systems that contain biological ligand motifs and operate in aqueous solution, covering some reactivity gaps that persist in synthetic models (Fig. 1).[22–24,26–28] While prior work studied the overall cluster across different ligand-bound and oxidation states, providing insight into key elements required for CO binding, we were unable to resolve the electronic structure of the individual sites. As such, the underlying basis for the high degree of selectivity and reactivity seen in native CODH remained elusive (Fig. 1).

Iron–sulfur clusters have complex electronic structures that are difficult to interpret without the use of multiple complementary, high resolution spectroscopies.[2,29,30] While the presence of many sites generally makes it difficult to determine the electronic structure of the individual iron centers, Mössbauer spectroscopy detects all $^{57}$Fe species, revealing the geometry, oxidation state, and spin state at the individual iron centers.[29,31–34] By applying a variable magnetic field during collection, the sign and magnitude of the hyperfine values for each iron center can be obtained, enabling interpretation of the complex spin-coupling schemes that dominate the electronic structure of iron–sulfur clusters in all redox states.[29,34–36] Coupling Mössbauer spectroscopy with additional techniques such as electron paramagnetic resonance (EPR) and high-energy-resolution fluorescence-detected X-ray absorption (HERFD-XAS) spectroscopies offers a complete picture of the electronic structure of heterometallic iron–sulfur clusters.[23,30,34,37–40] EPR spectroscopy generally selects for half-integer spin states (*e.g.*, $S = \frac{1}{2}$, $S = 3/2$), while the use of multiple frequencies provides a better understanding of high-spin species ($S > \frac{1}{2}$) by constraining the spin-Hamiltonian parameters. In addition, element-specific techniques such as HERFD-XAS selectively probe the nickel site, invisible to heterogeneity from residual homometallic clusters. Combining these techniques with computational models provides a complete understanding of the electronic structure of the whole system and provides a roadmap for future characterization of CODH intermediates.[41–45]

In this work, we combine Mössbauer, multifrequency X- and pulsed W-band EPR, and HERFD-XAS spectroscopic investigations on the reduced, oxidized, CO- and CN-bound NiFd clusters with quantum mechanics/molecular mechanics and broken-symmetry DFT calculations to determine how the different oxidation and ligand-bound states of NiFd influence the electronic structure of the cluster and individual iron sites. We have fully resolved the nature of the oxidized NiFd cluster, which represents a high-fidelity model of the cubane in the as-isolated $C_{ox}$ state of the CODH C-cluster. Comparison to the reduced NiFd cluster ($NiFd_{red}$), which models the cubane subsite of the $C_{red1}$ state of CODH, demonstrates how the cluster structure supports facile redox state transitions by delocalizing charge through the bridging sulfide ligands. Moreover, we have developed a unique spin coupling model for the NiFd–CO state that highlights exceptionally weak exchange interactions between the Ni–CO center and the $[Fe_3S_4]$ subcluster, with implications for understanding charge distribution in crucial catalytic intermediates in CO activation and $CO_2$ reduction. Ultimately, we hypothesize that the ligand-dependent, variable intracluster interactions may be essential for reproducing the desirable reactivity and selectivity of CODH.

## Results

### Multifrequency EPR spectroscopy constrains the spin-Hamiltonian parameters of $NiFd_{red}$ and NiFd–CO

One-electron reduction of the NiFd cluster produces a paramagnetic species ($NiFd_{red}$) that is readily observable using EPR spectroscopy. At X-band frequencies (9.37 GHz), this species exhibits a rhombic signal ($E/D > 0$) with major features at $g_{app} =$ 5.7, 5.0, 2.7 and 1.9, consistent with that of a high-spin, $S_{tot} = 3/2$ cluster (Fig. 2A). This species has previously been characterized and simulated at X-band frequencies with spin Hamiltonian parameters $g_{iso} = 2.0$ and $E/D = 0.16$.[23,24] Addition of CO to the headspace of the reduced NiFd results in a complicated spectrum with additional resonances around $g \sim 4$ and $g \sim 2$ (Fig. 2B). These features have been assigned to a single species with a ground spin-state $S_{tot,GS} = \frac{1}{2}$ and a low-lying excited state ($S_{tot,ES} = 3/2$) that is readily populated at temperatures as low as 5 K. Residual signal belonging to the $NiFd_{red}$ species is attributed to low solubility of CO in aqueous media and modest binding affinity of CO to the NiFd cluster, which we estimate to have a $K_d > 1$ mM on the basis of pressure-dependent experiments (Fig. S24). Temperature-dependent spectra of the NiFd–CO species show a small but nearly monotonic change in relative populations of the $S = \frac{1}{2}$ and $S = 3/2$ states between 4.5–15 K (Table S1). The $S = \frac{1}{2}$ state exhibits a similar asymmetrically broadened lineshape and temperature-dependent behavior as the $[Fe_3S_4]^+$ Fd (Fig. S1), which suggests the metal–metal exchange coupling of the NiFd–CO is subject to spin canting.[34,40,46,47]

Performing EPR experiments at higher fields and frequencies, such as the 34 GHz Q- and 94 GHz W-bands, provides increased resolution of g-tensor anisotropy and additional information on high-spin systems with zero-field splitting tensors larger than the microwave quanta at X-band ($D > 0.3$ cm$^{-1}$). Given our initial estimates on $D$, we decided to obtain echo-detected field-swept (EDFS) spectra at W-band on the high-spin $NiFd_{red}$ and NiFd–CO species to more accurately resolve the spin-Hamiltonian parameters.[24,25] To avoid the challenges

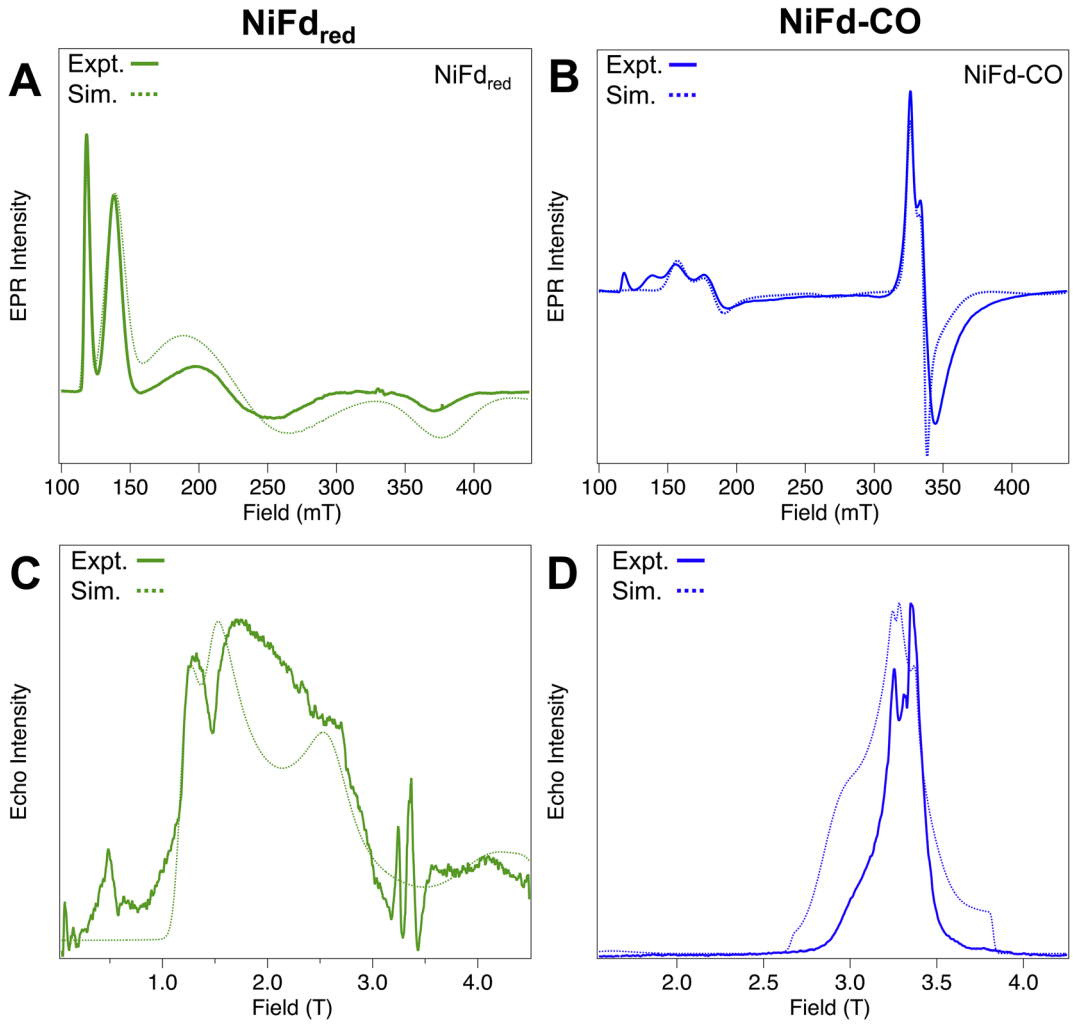


Fig. 2 (A) and (B) X-band CW EPR spectra ($\nu = 9.37$ GHz, $T = 8$ K, $P_{\mu w} = 20$ mW) of (A) $NiFd_{red}$ and (B) NiFd–CO. (C) and (D) Hahn-echo-detected pulsed W-band EPR spectra ($\nu = 94$ GHz; $T = 5$ K) of (C) $NiFd_{red}$ and (D) NiFd–CO. Dashed lines indicate simulated spectra. Experimental parameters: $\pi/2 = 32$ ns, $\tau = 260$ ns.

associated with rapid relaxation of high-spin species, the high-power, low-deadtime HiPER instrument at the U.S. National High Magnetic Field Laboratory was used.[48,49]

The W-band echo-detected field-swept (EDFS) spectrum of $NiFd_{red}$ exhibits broad intensity from 0.5–4.5 T (Fig. 2C). In order to determine which signals can be attributed to the $NiFd_{red}$ species, microwave nutation and relaxation experiments were performed at four different magnetic field positions along the absorption envelope (Fig. S2–S4). Extremely fast $T_1$ and $T_2$ relaxation rates, with lifetimes of ~2 μs and 100 ns, respectively, and similar nutation profiles are observed at all field positions, suggesting that the signals arise from a common, high-spin system. The nutation frequency of ~30 MHz is consistent with an $S = 3/2$ species (Fig. S4), based on comparison to an $S = \frac{1}{2}$ species that exhibited a nutation frequency of ~12 MHz (Fig. S21). Unfortunately, the rapid relaxation further indicated that additional pulsed EPR measurements, such as ENDOR or ESEEM, would likely be intractable. The X- and W-band EPR experimental spectra are simultaneously simulated as a $S_{tot} = 3/2$ species with a near-axial g-tensor, $g = [1.92\ 1.97\ 1.93]$, rhombicity of $E/D = 0.17$, and zero-field splitting principal component $D = -2.5\ cm^{-1}$ (Fig. S5–S7). These values are consistent with previous results, albeit resolved with higher confidence.[23] Because of the complexity of simulating and interpreting the X-/W-band EPR spectra of $NiFd_{red}$ and NiFd–CO, an in-depth discussion on selected simulation parameters and further analysis has been provided in the SI.

Unlike the $NiFd_{red}$ spectrum, the W-band EPR spectrum of NiFd–CO species only exhibits intensity in a narrow range from 2.8–3.6 T (Fig. 2D), though the spectrum is more complex than expected for a single $S = \frac{1}{2}$ species.[41] Notably, the low-field transitions seen at X-band frequencies near $g$ ~4 are absent at these fields, suggesting the spin Hamiltonian is dominated by the electronic Zeeman term and not the ZFS term. This necessitates a small energy separation of the spin ladder, as the microwave energy at W-band is ~3 $cm^{-1}$. In order to simulate this data in conjunction with the X-band spectra, we constructed a spin-coupled model that contains an $[Fe_3S_4]^0$ fragment coupled to the $Ni^+$-CO site. The magnitude of the effective electronic exchange interaction ($J_{eff}$) is proportional to the energy difference between the ground and excited states, while the sign of $J_{eff}$ determines the lowest energy ground state (Fig. S8–S9):

$$J_{eff} \propto E_{ex} - E_{gs}$$

Using this model, the spectra are best simulated as a spin-coupled system with an $S = \frac{1}{2}$ $Ni^+$ center having intrinsic $g = [2.32\ 2.22\ 2.09]$ and an $S = 1$ $[Fe_3S_4]^0$ system with intrinsic $g = [2.01\ 2.04\ 2.06]$, $D = +0.84\ cm^{-1}$, and $E/D = 0.052$ (Fig. S8). The value of $J_{eff}$ therefore represents the degree of exchange interaction between the $Ni^+$ center and the $[Fe_3S_4]^0$ subsystem, which we found to be antiferromagnetically coupled ($J_{eff} = -1.0\ cm^{-1}$). This results in a spin ladder with two populations at 5 K, an $S_{tot,GS} = \frac{1}{2}$ ground state (44%) with projected values of $g = [1.91, 1.99, 2.05]$ and an $S_{tot,ES} = 3/2$ exited state (56%) with projected values of $g = [2.12, 2.09, 2.07]$ and $D_1 = -0.079\ cm^{-1}$, $D_2 = -0.107\ cm^{-1}$, $D_3 = 0.187\ cm^{-1}$ (Fig. S10–S18). The simulation provides an acceptable fit to the data at both X- and W-bands (Fig. 2B and D), and the relative populations of the $S_{tot,GS} = \frac{1}{2}$ and $S_{tot,ES} = 3/2$ states are also consistent with the results observed at X-band (Tables S1 and S2). Relaxation experiments performed at 3.25 T resulted in longer $T_1$ and $T_2$ relaxation rates than the $S_{tot} = 3/2$ $NiFd_{red}$, with lifetimes of ~130 μs and 250 ns, respectively (Fig. S19). While $S = \frac{1}{2}$ species generally have slower $T_1$ and $T_2$ relaxation owing to the absence of low-lying excited states, there are many additional contributing factors that may affect relaxation.[43] Nutation experiments across the absorption envelope give frequencies of ~12 MHz and ~40 MHz, suggesting that the features from 3.24 T to 3.41 T may derive from two contributing spin systems, the previously proposed $S_{tot,GS} = \frac{1}{2}$ ground and $S_{tot,ES} = 3/2$ excited states (Fig. S20 and S21).

## Mössbauer spectroscopy probes the individual iron sites and interactions between metal centers

Mössbauer spectroscopy was used to define the oxidation states, spin states, and intracluster coupling within the $[Fe_3S_4]$ subcluster across the NiFd redox and ligand-bound series. Measurements performed at low temperatures in variable parallel applied magnetic fields enabled us to establish how electron redistribution and metal–metal coupling evolve upon reduction/oxidation and binding of $CN^-$ or CO. Detailed fitting procedures and coupling models are provided in the SI. Sample optimization and quality was verified using EPR spectroscopy before data collection (Fig. S22–S24). Mössbauer spectra of the reference $[Fe_3S_4]^{+/0}$ ferredoxin species closely match previously reported parameters,[29,32–34,40] confirming the expected all-ferric and mixed-valent electronic structures, respectively (Fig. S25, S26A, S27 and Table 1). The spectra of $[Fe_3S_4]^+$ and $[Fe_3S_4]^0$ were used to identify contaminants in NiFd samples as shown in the SI, Fig. S26B, C and S28–S30.

The reduced NiFd species, $NiFd_{red}$, exhibits a paramagnetically broadened spectrum at 1 kG, consistent with a half-integer spin state of $S_{tot} = 3/2$ (Fig. 3, green). After subtraction of residual $[Fe_3S_4]^0$ Fd from the spectra, we determined that $NiFd_{red}$ accounted for ~50% of the sample. The $NiFd_{red}$ species is best described as having a delocalized, mixed-valent $Fe^{2.5+}$ pair antiferromagnetically coupled to a third ferric site, indicating substantial electron delocalization within the $[Fe_3S_4]$ subcluster upon incorporation of nickel (Table 1, Fig. S26B and S28).[33] Analysis of the spectra suggests that two iron centers form a double-exchanged $S' = 9/2$ dimer, with the third iron center in antiparallel alignment.

The one-electron oxidation of $NiFd_{red}$ yields $NiFd_{ox}$. In an applied magnetic field of 1 kG, the Mössbauer spectrum of $NiFd_{ox}$ consists of a set of nested doublets with small quadrupole splittings centered at ~0.4 mm $s^{-1}$ (Fig. 3, black). After subtracting contributions from $[Fe_3S_4]^0$ Fd, $[Fe_3S_4]^+$ Fd, and $NiFd_{red}$ contaminants (Fig. S29), the $NiFd_{ox}$ complex is best described as having a total spin of $S_{tot} = 1$, with an $E/D = 0.22$ ($D = -1.9\ cm^{-1}$). Two iron sites, $Fe_1$ and $Fe_2$, have identical isomer

Table 1 Experimentally determined and DFT-calculated (in brackets) Mössbauer parameters for Pf NiFd from this work[a]

| Species | $D$ (cm$^{-1}$) | $E/D$ | $J_{iso}$ | $S$ | Site (s) | $\delta$ (mm s$^{-1}$)[b] | $\Delta E_Q$ (mm s$^{-1}$) | $\eta$ | $A_x$ (kG) | $A_y$ (kG) | $A_z$ (kG) | $A_{iso}$ |
|---|---|---|---|---|---|---|---|---|---|---|---|---|
| $[Fe_3S_4]^+$ Fd[c] | — | — | — | 1/2 | 1 | 0.27 (0.03) | 0.54 (0.03) | * | * | * | * | — |
| | | | | | 2 | 0.27 (0.03) | 0.54 (0.03) | | | | | |
| | | | | | 3 | 0.27 (0.03) | 0.54 (0.03) | | | | | |
| $[Fe_3S_4]^0$ Fd[e] | −2.4 (0.1) | 0.22 (0.02) | — | 2 | 1 + 2 | 0.47 (0.02) | 1.47 (0.07) | 0.44 (0.04) | −119 (7) | −198 (5) | −119 (2) | −145 |
| | | | | | 3 | 0.31 (0.04) | 0.50 (0.04) | 0.30 (0.02) | 118 (5) | 123 (5) | 113 (10) | 118 |
| $NiFd_{ox}$[d] | −1.9 (0.2) | 0.22 (0.02) | — | 1 | 1 + 2 | 0.46 (0.04) [0.31] | 1.33 (0.02) [1.38] | — | −220 (10) | −164 (12) | −17 (5) | −134 [−141] |
| | | | | | 3 | 0.35 (0.05) [0.23] | 0.85 (0.05) [−0.48] | — | 193 (10) | 181 (10) | 110 (10) | 161 [164] |
| $NiFd_{red}$ | −2.2 (0.02) | 0.18 (0.02) | — | 3/2 | 1 | 0.50 (0.05) [0.35] | −1.4 (0.2) [1.11] | −4.7 (0.6) | −131[h] | −182 (4) | −164 (3) | −159 [−106] |
| | | | | | 2 | 0.50 (0.05) [0.41] | −1.4 (0.2) [1.31] | −5.7 (0.6) | −131[h] | −182 (4) | −176 (5) | −163 [−102] |
| | | | | | 3 | 0.50 (0.05) [0.41] | −1.4 (0.2) [1.30] | −3.4 (0.5) | 109 (11) | 138 (2) | 132 (2) | 126 [106] |
| NiFd-CN[g] | +3.74 (0.4) | 0.03 (0.01) | — | 3/2 | 1 + 2 | 0.53 (0.03) | −1.23 (0.1) | −1.3 (0.1) | −116 (3) | −190 (3) | −180 (5) | −162 |
| | | | | | 3 | 0.53 (0.07) | −0.90 (0.2) | −2.0 (0.5) | 80 (3) | 139 (5) | 60 (15) | 93 |
| NiFd–CO[f,i] | +0.80 | 0.06 | 1 | 1/2 | 1 + 2 + 3 | 0.45 [0.31] | 1.2 [1.0] | 1.0 | −50 | −305 | −10 | −122 [−18] |

[a] Where possible, error bars are listed in parentheses. Calculated values are listed in square brackets. [b] Isomer shifts are quoted relative to Fe metal at 298 K. Linewidths are 0.35 mm s$^{-1}$ for all components of the simulation. [c] Quadrupole splitting and isomer shift parameters for $[Fe_3S_4]^+$ Fd were modeled after those reported for $[Fe_3S_4]^+$ Fd from *D. gigas* in ref. 40 and * denotes values for which $\eta$ and hyperfine parameters are not reported. [d] $\alpha_{EFG,Site1} = 80\ (\pm5)°$; $\beta_{EFG,Site1} = 100\ (\pm5)°$. [e] $\beta_{EFG,Site1} = 18\ (\pm2)°$; $\beta_{EFG,Site3} = 105\ (\pm5)°$; $\gamma_{EFG,Site3} = 85\ (\pm3)°$. [f] $\alpha_{EFG,Site1} = 34°$; $\beta_{EFG,Site1} = 154°$; $\gamma_{EFG,Site1} = 150°$; $D$, $E/D$, and $J$ were constrained by simulation of temperature-dependent EPR data. [g] No calculations were performed on the NiFd-CN species. [h] Error bars could not be accurately determined for these parameters. [i] Error bars could not be reliably determined for the CO-bound species due to strong parameter interdependence in the Hamiltonian.




Fig. 3 Mössbauer spectra of $NiFd_{ox}$ (black), $NiFd_{red}$ (green), NiFd-CN (orange), and NiFd–CO (blue) at $T = 4.2$ K in an applied magnetic field of 1 kG. Contributions from known $[Fe_3S_4]$ species have been subtracted.

shifts and quadrupole splittings ($\delta = 0.46$ mm s$^{-1}$, and $\Delta E_Q = 1.33$ mm s$^{-1}$) that are consistent with a mixed valent delocalized $Fe^{2.5+}$ pair. In strong applied magnetic fields, the two cluster types yield distinct spectra, with hyperfine values suggesting that these two sites are aligned antiparallel to the third iron site, $Fe_3$, ($\delta = 0.35$ mm s$^{-1}$, and $\Delta E_Q = 0.85$ mm s$^{-1}$), to yield a subcluster spin of $S = 2$, which then antiferromagnetically couples to the $S = 1$ $Ni^{2+}$ site, resulting in an overall spin $S_{tot} = 1$. The Mössbauer parameters used to simulate the experimental spectra are shown in Table 1, with the full spectral fitting presented in Fig. 4. The hyperfine coupling constants for site 3 are more isotropic compared to sites 1 + 2, implying a different ligand field or magnetic coupling environment. In the high-field Mössbauer spectra shown in Fig. 4B–D, Fe site 3 mainly contributes to the spectral shoulders near ±3 mm s$^{-1}$ and ±4 mm s$^{-1}$, while the combined signal from sites 1 + 2 accounts for most of the intensity in the middle of the spectra. Together, these features are indicative of a cluster with an overall delocalized electronic structure, consistent with a $[Fe^{2.5+}$–$Fe^{2.5+}$–$Fe^{3+}]$ formulation as shown in Fig. 8.

Binding of the CODH C-cluster inhibitor, $CN^-$, to $NiFd_{red}$ is quantitative, with a dissociation constant $K_d \sim 160$ μM determined from EPR studies (Fig. S23 & S26C). Cyanide binding to the nickel center only slightly perturbs the electronic structure at the iron sites, as seen by the minor changes in the Mössbauer parameters relative to $NiFd_{red}$ (Fig. 3, orange, Table 1).[25] The modest increase in isomer shift suggests slightly increased charge density at the iron sites upon binding cyanide. Nevertheless, Mössbauer parameters used to fit the NiFd-CN spectra remain consistent with those previously published by Srivastava *et al.*, and the system is best described with a $S_{tot} = 3/2$ ground state.[24,33]

Finally, binding of CO to $NiFd_{red}$ yields NiFd–CO, which exhibits significantly narrower spectra, consistent with a lower

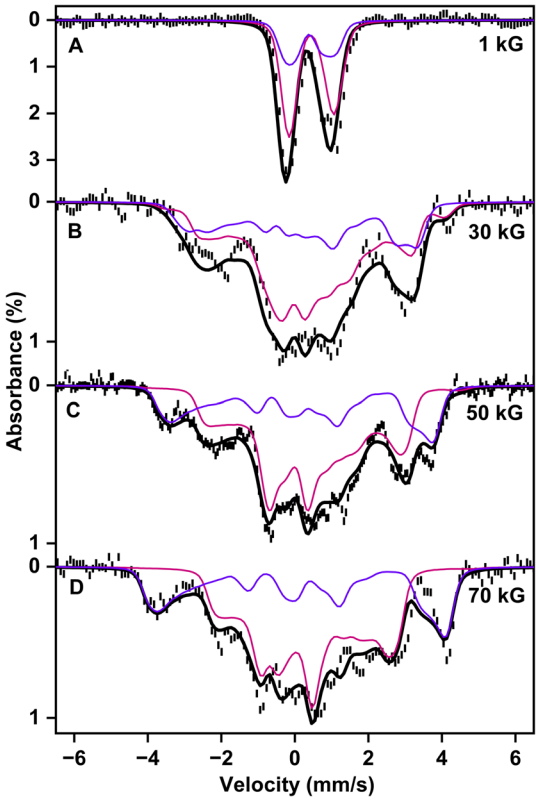


Fig. 4 Mössbauer spectra of $NiFd_{ox}$ collected at 4.2 K in parallel applied magnetic fields of (A) 1 kG, (B) 30 kG, (C) 50 kG, and (D) 70 kG. The black dashed traces represent the difference spectra obtained after subtracting contributions from ~34% $[Fe_3S_4]^+$, ~15% $NiFd_{red}$, and ~9% $[Fe_3S_4]^0$. The resulting spectra correspond to ~42% $NiFd_{ox}$. The solid black lines show the overall simulation, while the magenta and violet curves represent the individual contributions from Fe sites 1 + 2 and Fe site 3, respectively. Mössbauer parameters used for the magenta and violet traces are listed in Table 1.

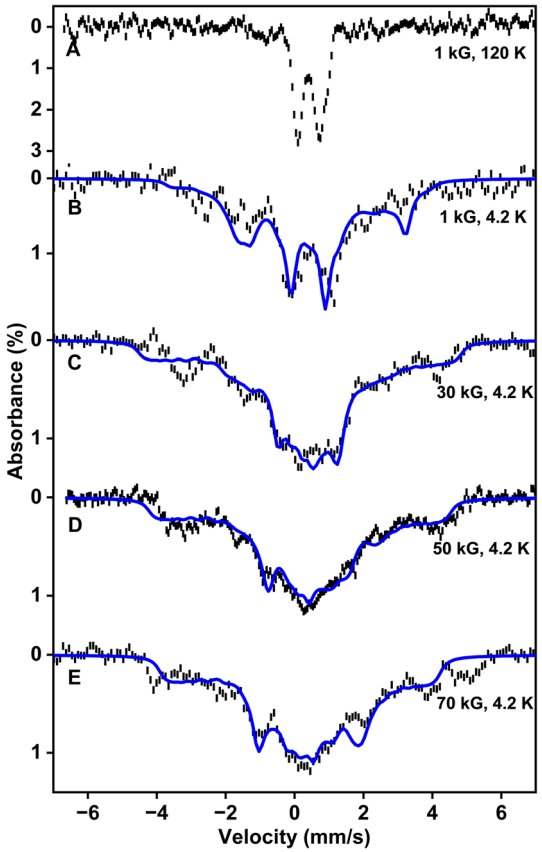


Fig. 5 Mössbauer spectra of NiFd–CO collected at 120 K (A) and 4.2 K (B–E) in parallel applied magnetic fields of (A and B) 1 kG, (C) 30 kG, (D) 50 kG, and (E) 70 kG. The black hash marked spectra represent the difference spectra, corresponding to 40% NiFd–CO, obtained after subtraction of 45% $[Fe_3S_4]^0$ (experimental data) and ~15% $NiFd_{red}$ (simulation). The blue curves are simulations of the experimental difference spectra. Parameters used to generate the blue curves are presented in Table 1.

spin state ($S < 3/2$) (Fig. 3, blue, Fig. 5, Table 1). Due to the low binding affinity of CO to $NiFd_{red}$ (Fig. S24), the species of interest (NiFd–CO) accounted for 40% of the total sample. In addition to the low yield of the CO-bound species, analysis of the data is complicated by the presence of a low-lying $S = 3/2$ excited state that is appreciably populated, even at 5 K (Fig. S18, S30, S31, Tables S1 and S2). However, the fast electronic spin relaxation observed in the high temperature ($T =$ 120 K) data collected for NiFd–CO and the symmetry of the spectrum provides insight into the homogeneity of the iron sites in the cluster and serves as the rationale to treat the iron sites as equivalent in the analysis described below (Fig. 5). These data also constrain the isomer shift and quadrupole splitting to $\delta = 0.45$ mm s$^{-1}$ and $\Delta E_Q = 1.2$ mm s$^{-1}$ (Fig. S32), values that are comparable to those obtained for the reduced cluster.

The presence of a low-lying excited state prevents the Mössbauer spectra of the CO-bound species from being fit using a simple description of the iron sites in the cluster with a total spin defined for the system, as was done for other NiFd species (Fig. S31). This is because the coupling between the sites in the cluster is weak, and the cluster does not exhibit a well-isolated ground state. Instead, fitting the Mössbauer spectra presented here required consideration of contributions from both the ground and excited states *via* a two-spin model. Reasonable simulations of the difference spectra of NiFd–CO (Fig. 5) are best described in a spin-coupled representation provided that we: (i) take the average Mössbauer parameters for all Fe sites at a relative spectral area contribution of 1.0, and (ii) that we model the second site in the spin coupling model as an $S = 1/2$ site (with no explicit spectral contribution in the Mössbauer data). Based on these assumptions and the overall spin state of the complex, we propose that NiFd–CO is composed of a $[Fe_3S_4]^0$ subcluster with total spin $S = 1$ that is aligned antiparallel to a $S = 1/2$ $Ni^+$-CO site. A more detailed description of this configuration is described in the Discussion section (*vide infra*). In short, the Mössbauer data were fit assuming a total spin of $S_{tot} = 1/2$ (with isotropic exchange coupling constant, $J = 1.0$ cm$^{-1}$), whereas the ferromagnetic coupling of the sites would yield a total ground spin of $S_{tot} = 3/2$. The energy level diagram corresponding to this description is shown in Fig. S8 and S9.

While we acknowledge that taking the average of the Mössbauer parameters for the three iron sites in the cluster and

treating them as a single site, even in strong applied magnetic fields, introduces an inherent limitation in our analysis, it was the most tractable simulation and calculation approach that we could reasonably achieve. Additionally, inclusion of multiple, distinct iron sites did not improve the quality of the fits. It is also worth noting for the reader that there are several soft parameters that could not be uniquely determined but are reported as the values used to generate the simulated spectra presented herein. Nevertheless, the Mössbauer analysis presented here offers a valuable framework for future analyses in the field.

### High-energy-resolution fluorescence-detected X-ray absorption spectroscopy (HERFD-XAS) on the nickel site in NiFd

To complement the highly resolved information on each of the Fe centers in NiFd obtained using Mössbauer spectroscopy, we performed high-energy-resolution Kα fluorescence-detected X-ray absorption spectroscopy (HERFD-XAS) at the nickel and Fe K-edges on the different states of NiFd (Fig. 6 and S34). This technique suppresses the lifetime broadening of the 1s core-hole and provides far superior experimental resolution of the metal pre-edge features than total fluorescence yield (TFY) XAS (Fig. S33–S38). As a result, overlapping 1s → 3d and charge-transfer transitions can be separated, permitting better comparison across different states and to theory. The rising edge positions can also be resolved more clearly, providing a more robust measurement of element-specific electron density. While the Fe Kα HERFD-XAS spectra of WT NiFd show only minor changes across all of the species (Fig. S34), the Ni Kα HERFD spectra show clear distinctions between the oxidized and reduced states, including changes in pre-edge feature intensity, number, and edge energy (Tables S3 and S4). Specifically, the pre-edge transitions split from one peak in the reduced state to two resolved features in the oxidized species. This splitting was not resolved in the TFY-XAS and is consistent with the presence of two 3d acceptor orbitals, as would be expected for a tetrahedral, high-spin $Ni^{2+}$ center. The $NiFd_{red}$ species shows only one pre-edge feature and a red-shift of the edge position from 8342.3 eV in the oxidized sample to 8338.4 eV, consistent with a more electron-rich $Ni^{+}$ center (Fig. 6). The ~4 eV shift in edge position suggests a large change in covalency along with electron density at the nickel site, with shifts of this magnitude previously reported in XAS studies of other nickel metalloproteins and synthetic complexes.[50–52]

For the NiFd–CO species, the rising edge position shifts to higher energy by almost 1 eV relative to $NiFd_{red}$, but remains significantly lower than that of the $NiFd_{ox}$ species, justifying the formal assignment as a $Ni^{+}$ center (Table S3). We attribute the lower electron density at the nickel center to π-backbonding into the CO ligand, which is consistent with resonance Raman data showing a high degree of activation for the bound CO ($\nu_{CO}$ = 1964 $cm^{-1}$).[25] A new pre-edge feature for NiFd–CO is also observed at 8334.4 eV, almost 2 eV higher in energy than the pre-edge feature of $NiFd_{red}$. The shift of this 1s → 3d transition to higher energies is consistent with the increased ligand field strength expected for a CO-bound species. In contrast to the NiFd–CO species, the pre-edge intensity of the NiFd-CN species decreases significantly, and the edge position shifts hypsochromically to align with the $NiFd_{ox}$ species. The associated formation of a sharp feature at ~8336 eV can be attributed to a 1s → 4p transition. Collectively, as noted previously, these observations are consistent with geometric rearrangement to yield a low-spin, square-planar $Ni^{2+}$ center with large 3d–4p mixing.

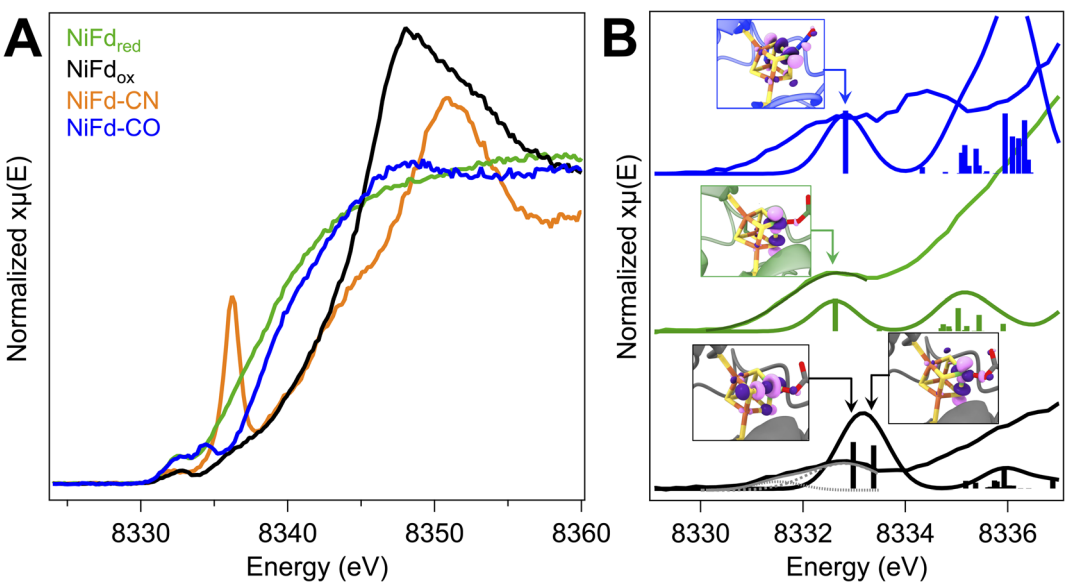


Fig. 6 (A) Ni Kα HERFD-XANES spectra of NiFd in the oxidized (black), reduced (green), CO-bound (blue) and CN-bound (orange) states. (B) Zoomed-in view of the pre-edge region for the oxidized and reduced NiFd and NiFd–CO compared to TD-DFT calculated transitions. Gaussian peak decompositions are indicated in grey and dark green for $NiFd_{ox}$ and $NiFd_{red}$, respectively. Natural transition orbitals (NTOs) are shown for the dominant pre-edge transitions for each species. Spectra and stick transitions are offset for clarity.

### Broken-symmetry density functional theory (BS-DFT) investigations of NiFd electronic structure

Using the published crystal structure (PDBID: 2Z8Q) of the Pf D14C $Fe_4S_4$ ferredoxin, computational models of the $NiFd_{red}$, $NiFd_{ox}$, and NiFd–CO states were built, with extensive equilibration used to provide reasonable structures for analysis. Median structures were then subjected to a QM/MM optimization in the broken-symmetry density functional theory (BS-DFT) formalism. The oxidation states of the complex that were elucidated previously provide, for each state, three broken-symmetry ground states, each consisting of a Ni–Fe pair antiferromagnetically coupled to an Fe–Fe pair.[25] We denote here BS1, BS2, and BS3 as the broken-symmetry configurations that ferromagnetically pair Ni–$Fe_1$, Ni–$Fe_2$, and Ni–$Fe_3$ (Fig. 7A–C) to produce the ground state. These are the only ground states that can be constructed with all sites locally high spin. The lowest energy QM/MM broken-symmetry geometry was chosen for further analysis (Table S5). For the $NiFd_{red}$ and $NiFd_{ox}$ states, the BS3 geometry was lowest in energy, and for NiFd–CO, BS1 was lowest in energy (Fig. 7 and Table S5). At these geometries, spin ladders were constructed using the high-spin (all sites ferromagnetically coupled) and three broken-symmetry ground states. The spin-ladders reflect the interdependence between geometry and electronic structure, with BS3 being lowest in energy for $NiFd_{red}$ and $NiFd_{ox}$, and BS1 being lowest in energy for NiFd–CO when single point calculations were performed (Table S5). For $NiFd_{red}$, the BS1, BS2, and high-spin states were 7.4, 6.6, and 23.0 kcal $mol^{-1}$ higher than BS3. $NiFd_{ox}$ had a similar ordering of states, with the respective spacings for BS1, BS2, and high-spin at 4.1, 2.7, and 33.7 kcal $mol^{-1}$ above the lowest energy spin configuration (Table S5). The alternative lowest energy spin configuration in NiFd–CO resulted in BS2, BS3, and the high-spin state at 11.7, 5.5, and 22.3 kcal $mol^{-1}$ above the computed ground state (Table S5). Neither removal of point charge embedding for any NiFd state nor a trial larger QM region for $NiFd_{red}$ changed the preferred BS configuration (Table S5). This permitted the use of a primary-sphere QM region for further analysis of the electronic structure.

Natural population analysis (NPA) shows that upon reduction of $NiFd_{ox}$ to $NiFd_{red}$, the negative charge on Ni increases by $\sim 0.2e$, while the charges on the bridging sulfide atoms in $Fe_3S_4$ increase by a total of $\sim 0.5e$. Little change to the charges on Fe are seen (Fig. 7D), though the cysteine thiolate sulfur atoms bear an increase in charge of $\sim 0.2e$. These findings are in line with the formal reduction process being dominated by the electronegativity of Ni and would be expected to increase covalency of the nickel site, as reflected in the substantial shift in HERFD-XAS edge position. The spin density at the Ni center also decreases in magnitude from −1.4 to −1.1, consistent with reduction of the high-spin $S = 1$ center to an $S = 1/2$ species. Binding of CO to $NiFd_{red}$ to give NiFd–CO shows a substantial charge decrease of $\sim 0.4e$ and spin decrease to −0.7 at the Ni center, along with decreased charge and spin at one of the Fe centers ($Fe_2$) (Table S5).

The lowest energy broken-symmetry states were used to calculate Mössbauer parameters, including $\delta$, $\Delta E_Q$, and $A_{iso}$ (Table 1), with augmented basis sets and established benchmarking used to accurately interpret core electron properties. The strongest agreement between experiment and BS-DFT is seen for the $NiFd_{ox}$ model. The computed isomer shift and quadrupole splitting agree well with experiment, featuring two distinct sets of Fe centers in the cluster, and the hyperfine parameters indicate that the two identical Fe centers are

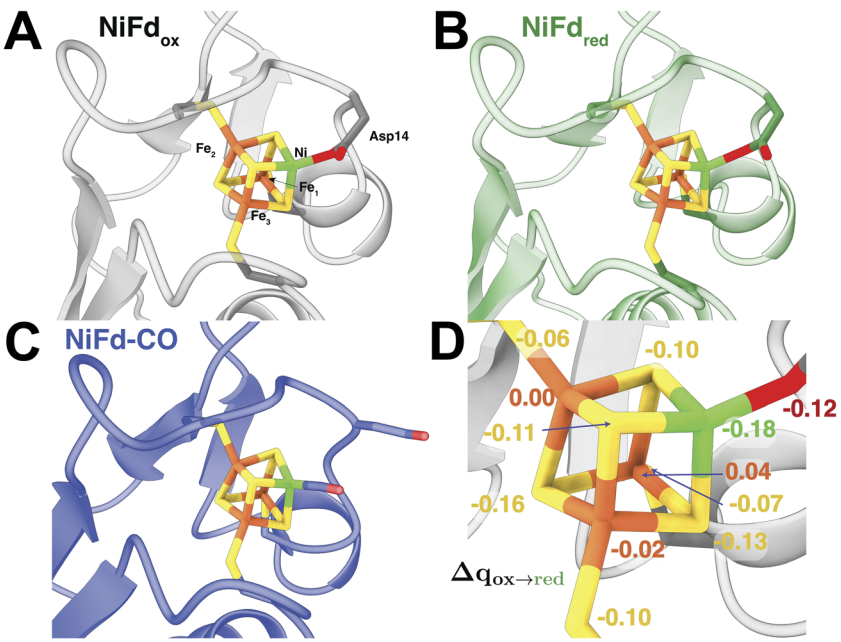


Fig. 7 Geometry-optimized QM/MM models of (A) $NiFd_{ox}$, (B) $NiFd_{red}$ and (C) NiFd–CO used in this study. (D) Change in charge from natural population analysis in going from $NiFd_{ox}$ to $NiFd_{red}$. Atoms and charge changes are colored as follows: Fe (orange); Ni (green); S (yellow); O (red).

antiferromagnetically coupled to a high-spin, ferric site. DFT calculations of these parameters for the high-spin states do not agree (Table S6), even qualitatively, with experimental trends, lending support to the model that the ground state of $NiFd_{ox}$ is well-described by a double-exchange coupled $Fe^{2.5+}/Fe^{2.5+}$ pair, antiferromagnetically (AF) coupled to a single $Fe^{3+}$ to give an $S = 2$ subcluster. The $S = 1$ $Ni^{2+}$ site is then AF-coupled to the $[Fe_3S_4]^0$ subcluster to result in the overall $S_{tot} = 1$ spin state for the entire cluster. Magnetic site–site J-couplings ($J_{ij}$) using the Heisenberg–Dirac–van–Vleck Hamiltonian were computed for the $NiFd_{ox}$ state including higher S states, as the BS determinant showed strong agreement with experiment, giving an effective $J_{eff} = -158\ cm^{-1}$ between the $S = 1$ Ni and $S = 2$ Fe subsite (Table S7 and Fig. S39). Calculated Mössbauer parameters for $NiFd_{red}$ show qualitative agreement with the experimental Mössbauer spectra, having two identical Fe sites antiferromagnetically coupled to a third Fe, but the near-quantitative agreement is lost. Here, $\delta$ and $\Delta E_Q$ show a similar 2 + 1 pairing of Fe sites as seen in $NiFd_{ox}$. Calculations on the NiFd–CO state gave average values for $\delta$ and $\Delta E_Q$ that are in reasonable agreement with experiment, but given the complexity of the electronic structure of that state (*vide infra*), the site-specific values are not necessarily expected to align well with experiment (Table 1).

To complement examination of the electronic structure of the Fe centers, the Ni K-edge X-ray absorption pre-edge features were calculated with time-dependent density functional theory (TD-DFT), using specialized inputs to probe core orbital excitations.[53,54] The lowest energy BS states were used to excite Ni core electrons to the valence shell. Natural transition orbitals (NTO) were computed to identify the dominant source of the transitions and confirm the identity of pre-edge features (Fig. 6B, inset). The first pre-edge feature in $NiFd_{red}$ is identified as a quadrupole-allowed 1s → 3d transition, with a high contribution from the Ni $3d_{z^2}$ orbital. The maximum of the $NiFd_{ox}$ peak is shifted to higher energy relative to $NiFd_{red}$. Similarly, two dominant peaks are predicted with high contributions in the NTOs from orthogonal Ni 3d orbitals that resemble the Ni $3d_{x^2-y^2}$ and $3d_{z^2}$ orbitals. These match the assignment of a physical $Ni^+$ and $Ni^{2+}$ site in $NiFd_{red}$ and $NiFd_{ox}$, respectively, corresponding to suggested interpretations from previous work.[25] The NiFd–CO pre-edge is calculated to be more intense and blue-shifted by ~0.2 eV relative to the $NiFd_{red}$ pre-edge feature. The peak for NiFd–CO originates from a 1s → $3d_{z^2}$ transition with mixing into the C 2p orbital, similar to the other states but with a rotated *z*-axis relative to $NiFd_{red}$ (Fig. 6B). The calculations significantly underestimate the energy shift of the pre-edge feature but do reproduce the intensity increase seen experimentally.

No calculations were performed on the NiFd-CN, which is suggested from the XAS to undergo substantial geometric rearrangement at the nickel center to form a localized, low-spin $Ni^{2+}$ site. Additional approaches are being developed to validate electronic structures and geometries of NiFd-CN and related systems in order to computationally characterize these mixed-spin clusters.

# Discussion

### Element-specific electronic structure reveals cluster redox plasticity in NiFd and ligand involvement in modulating charge distribution

In an earlier study that explored redox-state changes and ligand binding to NiFd species,[23] it was suggested that the majority of electronic changes occurred at the Ni center, though the extent to which the electron density was distributed around the cluster was unresolved. This was largely attributed to the minor changes in the Fe K-edge XANES, which reflected a global average of all iron centers in the sample, and the high degree of covalency of the nickel sulfide site. In this work, variable-field Mössbauer spectroscopy and analysis coupled with the nickel K-edge HERFD-XAS and QM/MM studies provide a more complete picture of the changes occurring at all of the metal centers and the resultant charge that is buffered by the bridging sulfide and terminal thiolate ligands.

Like the $C_{ox}$ state in CODH, the $NiFd_{ox}$ species is EPR-silent, making it more challenging to characterize the electronic structure than the other, EPR-active states. Previously obtained results from the Ni XANES are consistent with the nickel center adopting a $Ni^{2+}$ oxidation state in a tetrahedral geometry leading to a local $S = 1$ spin state, though the spin state of the cluster remained unclear.[25] Using Mössbauer spectroscopy, the electronic structure picture of the iron sites can be resolved. The isomer shifts and quadrupole splittings of the three iron sites are only slightly perturbed upon incorporation of the $Ni^{2+}$ center when compared to the $[Fe_3S_4]^0$ cluster. In particular, the isomer shift of site 3 experiences a modest increase, which may suggest an increase in electron density at this site due to the covalency of the Fe–S–Ni bond. The similarities in the values at all three iron sites compared to the $[Fe_3S_4]^0$ cluster suggest that the cluster is comprised of a $Fe^{2.5+}$ mixed valent pair, aligned antiparallel to the ferric center (Fig. 8). The overall spin state, $S_{tot} = 1$, likely arises from the antiferromagnetic coupling of the high-spin $Ni^{2+}$ ($S = 1$) center to the $[Fe_3S_4]^0$-like $S = 2$ subcluster. Computational analysis supports this assessment, with calculated Mössbauer parameters from the lowest energy BS wavefunction showing a 2-Fe mixed-valence pair with similar isomer shifts and quadrupole splittings antiferromagnetically coupled to the third Fe center. The calculated effective exchange coupling of $J_{eff} = -158\ cm^{-1}$ between the $S = 1$ Ni and $S = 2$ Fe subcluster suggest a well-isolated $S = 1$ ground state, as observed experimentally, and the qualitatively correct spectroscopic parameters obtained from BS-DFT for $NiFd_{ox}$ indicate the method offers a reliable tool for elucidating the electronic structure.

Reducing the cluster gives an $S = 3/2$ total spin state, and on the basis of the Ni/Fe K-edge XAS data, we previously postulated that reduction of $NiFd_{ox}$ occurs primarily at the $Ni^{2+}$ center to form a $Ni^+$ center. However, the experimentally resolved isomer shifts ($\delta = 0.5\ mm\ s^{-1}$) and quadrupole splittings ($\Delta E_Q = -1.4\ mm\ s^{-1}$) for the three nearly equivalent iron centers in $NiFd_{red}$ increase to more closely resemble values associated with delocalized $Fe^{2.5+}$ centers.[29,55] In the analogous reduced

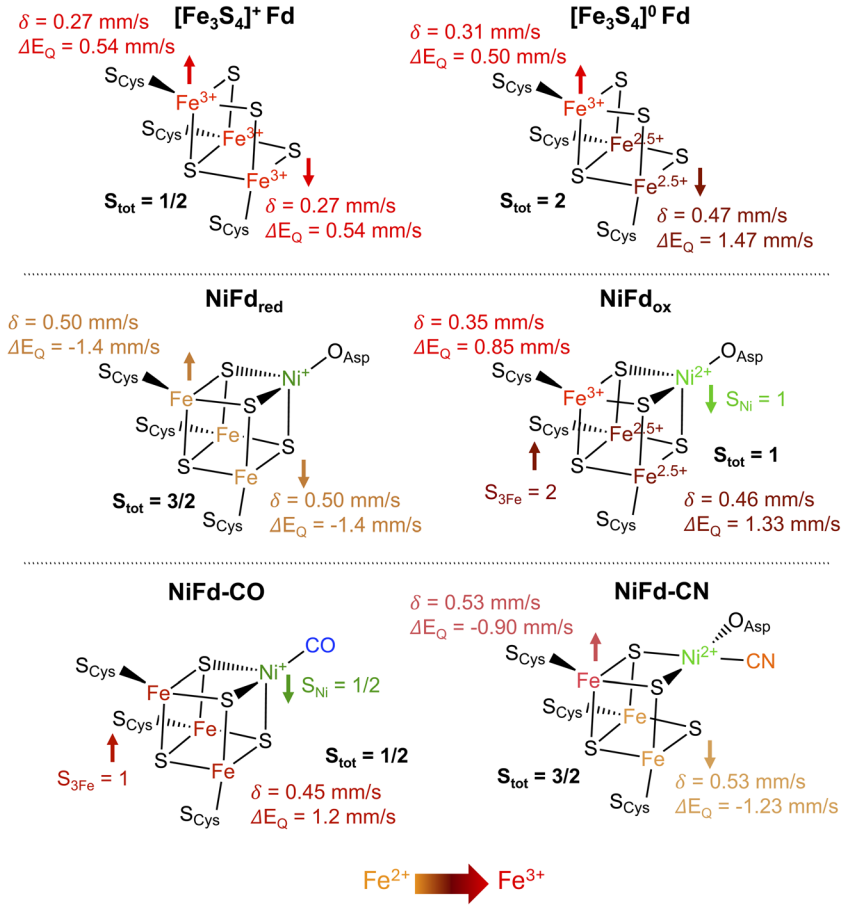


Fig. 8 Proposed electronic and geometric structures of Fd species with Fe charge density indicated as a heat map from red (ferric) to orange (ferrous) as assigned using EPR and Mössbauer spectroscopies.

$[Fe_4S_4]^+$ cluster, the system is described as a double-exchange-coupled mixed valent dimer ($\delta$ ~0.49 mm s; $|\Delta E_Q| = 1.32$ mm $s^{-1}$) antiferromagnetically coupled to a ferrous dimer ($\delta$ ~0.58 mm $s^{-1}$; $|\Delta E_Q| = 1.89$ mm $s^{-1}$).[29] It is thus clear from the Mössbauer analysis of $NiFd_{red}$ that the third iron also becomes reduced, but less so than would be expected for a full one-electron reduction to an $Fe^{2+}$ center. This suggests that the Ni center accepts more electron density than all of the Fe centers. The ~4 eV red-shift in the edge position from the HERFD-XAS supports this conclusion, consistent with the formal $Ni^+$ oxidation state proposed in previous studies.[25]

However, it may be more appropriate to consider the change in charge distribution in terms of fractional values. NPA charges in the $NiFd_{ox}$ and $NiFd_{red}$ forms show that the electron density on Ni increases upon reduction to a greater extent than any individual other atom, but only by ~0.2*e*. Moreover, while the average calculated increase in the isomer shift of the Fe centers in $NiFd_{red}$ is 0.12 mm $s^{-1}$, the NPA shows minimal change in charge on the iron centers. Instead, nearly all of the remaining charge is compensated by increased density on each of the $\mu^3$-sulfide ligands and cysteine thiolates, and it is likely that this increase in ionic bonding character contributes to the increased isomer shift.[29,56] A recent study on a synthetic $Ni_2Fe_3S_4$ cluster has suggested the presence of metal–metal (Ni–Fe) bonding, which could have implications for synthetic and biological cubane clusters, including NiFd and CODH.[21,22] However, our previous Ni K-edge EXAFS data of all of the distinct NiFd species ($d_{NiFe}$ = 2.65–2.75 Å) found that Ni–Fe distances appear to be significantly longer than those observed for the synthetic $Ni_2Fe_3S_4$ cluster ($d_{NiFe}$ ~2.52 Å), and are comparable to the bond lengths observed in biological $[Fe_4S_4]$ clusters ($d_{FeFe}$ ~2.6–2.7 Å) and synthetic $[NiFe_3S_4]$ clusters ($d_{NiFe}$ ~2.69 Å) with "non-bonded" Ni–Fe centers such as the $[NiWFe_2S_4]$ cluster from the Holland group ($d_{NiFe}$ ~2.79–2.88 Å).[21,26,57,58] Although bonding-like orbitals were observed using Pipek–Mezey (PM) orbital localization (Fig. S40), they only exist for the Ni–Fe pair that is ferromagnetically coupled, and only observed in the $\alpha$ channel, for both $NiFd_{red}$ and $NiFd_{ox}$ species, as opposed to the doubly-occupied PM-localized bonding orbitals observed in previous works.[21,22,59] Further bonding analysis supports a lack of Ni–Fe bonding (SI). For this reason, we believe the covalency and electron density is mediated through the sulfide bridges and not directly through metal–metal bonds. The three iron centers are suggested to adopt the same physical oxidation state as each other, being more electron rich than in the $NiFd_{ox}$ state, though it is not straightforward to assign this numerical value and we refrain from doing so (Fig. 8). The multifrequency EPR data confirm the well-isolated ground spin state of $S_{tot} = 3/2$, in line

with the spin ladder calculations and the large calculated AF exchange coupling constants, and the zero-field splitting (ZFS) value obtained from the multifrequency EPR simulations is consistent with values obtained from Mössbauer spectroscopy.

The binding of $CN^-$ to $NiFd_{red}$ induces significant changes, as evidenced by the spectroscopic properties. The ground spin state remains as a well-isolated $S_{tot} = 3/2$ state, but the cluster adopts near-axial symmetry and the sign of the ZFS tensor inverts. The changes in the Ni K-edge HERFD-XAS spectra, including a decrease in pre-edge intensity, increase in the 1s → 4p transition, and blue-shift of the edge position to overlap with that of $NiFd_{ox}$, suggest that the Ni center adopts a low-spin, square-planar $Ni^{2+}$ configuration. The significant shifts in the XAS pre-edge and edge features, as well as previously obtained Ni K-edge EXAFS data confirm that $CN^-$ binds to the nickel center.[25] In this model, it is postulated that the extra electron density is distributed among the three remaining iron centers, which would be expected to lead to an overall increase in the average isomer shift of the three irons. However, these increases are minimal, with experimentally determined isomer shifts at $Fe_1$ and $Fe_2$ of $\delta = 0.53$ mm $s^{-1}$ reflecting an increase of 0.03 mm $s^{-1}$. The isomer shift at $Fe_3$ also shows a modest increase of 0.03 mm $s^{-1}$ ($\delta = 0.53$ mm $s^{-1}$), suggesting a minor increase in electron density (Fig. 8). Typically, the addition of one electron to an $[Fe_3S_4]$ cluster is associated with an overall summed increase in isomer shift of ~0.4 mm $s^{-1}$, which is much greater than the cumulative +0.15 mm $s^{-1}$ observed across the $[Fe_3S_4]$ fragment in NiFd-CN. While this small change does not account for all of the added expected electron density, iron–sulfur clusters are highly covalent in nature, which may result in the extra electron density being delocalized across the $CN^-$ ligand, bridging sulfides, and iron centers such that there is not a significant change in the isomer shift at all three irons. The cyanide ligand may also accept some electron density, though the FTIR band observed at 2050 $cm^{-1}$ is only slightly lower in energy than free $CN^-$ at 2080 $cm^{-1}$, suggesting weak π-accepting and stronger σ-donating character.[23]

Though $CN^-$ and CO are isoelectronic and generally considered to bind to metals in a similar manner, a growing body of work suggests that binding of CO and $CN^-$ to clusters differentially affect the electronic structure.[25,60] This is clearly borne out in the case of NiFd. Moreover, the binding affinities for $CN^-$ ($K_d$ ~160 μM) and CO to $NiFd_{red}$ ($K_d > 1$ mM) differ by at least one order of magnitude (Fig. S23 and S24), suggesting the electronic structure differences affect reactivity as well. The Mössbauer and multifrequency EPR spectroscopy indicate that the NiFd–CO species adopts a ground spin state of $S_{tot,GS} = 1/2$, with a low-lying $S_{tot,ES} = 3/2$ excited state, in contrast to the ground spin states of both $NiFd_{red}$ and NiFd-CN. The isomer shift of the iron sites ($\delta = 0.45$ mm $s^{-1}$) is lower than what is observed in the $NiFd_{red}$ cluster, with a shift in Ni K-edge position to higher energy, consistent with CO acting as a strong π-acceptor and depleting electron density from all the metal centers across the cluster. These observations along with the Ni K-edge XANES, edge position, NTO, and the CO vibrational frequency ($\nu_{CO} = 1964$ $cm^{-1}$) suggest CO binds directly to the nickel center, which remains in the formal +1 oxidation state.[25]

The $S_{tot,GS} = 1/2$ ground spin state is best explained by weak antiferromagnetic coupling between the $S = 1/2$ $Ni^+$ site to a $S = 1$ $[Fe_3S_4]^0$ fragment. The $S = 1$ spin state of the $[Fe_3S_4]^0$ subsite differs from the $S = 2$ ground spin state of the canonical $[Fe_3S_4]^0$ cluster (Table 1), though this is not unexpected given the distinct Mössbauer parameters observed. The unusual spin state and equivalence across the Fe sites implies that the subsite experiences spin canting, much like the oxidized $[Fe_3S_4]^+$ cluster, which may also explain the similarities in lineshape of the temperature-dependent EPR signatures of the NiFd–CO and $[Fe_3S_4]^+$ Fd (Fig. S1). Attempts to construct an $S_{tot} = 1/2$ state using broken-symmetry DFT, which employs a single, collinear spin determinant, do not reproduce the experimental parameters that are seen in the EPR and Mössbauer spectra for NiFd–CO (Table S6), further supporting a model in which spin canting must be invoked. As an alternate explanation, the approximately $C_{3v}$ symmetry around the cluster in the CO-bound state would likely give near-degenerate spin configurations. This is distinct from the structures in $NiFd_{ox}$ and $NiFd_{red}$, highlighting a limitation in the broken-symmetry method and calling for a multiconfigurational approach in future work. The X- and W-band temperature-dependent EPR simulations are consistent with the observed antiferromagnetic exchange coupling ($J_{eff} = -1.0$ $cm^{-1}$) determined from the Mössbauer simulations. This value is significantly lower than the site–site exchange couplings observed in other iron–sulfur clusters ($|J_{ij}| = 20$–$100$ $cm^{-1}$) and those computed for the $NiFd_{ox}$ ($J_{eff} = -158$ $cm^{-1}$).[32] The weak coupling observed between the Ni site and the $[Fe_3S_4]$ cluster fragment implies that in this state, the Ni center may behave more like a mononuclear system, while the $[Fe_3S_4]$ subsite may modulate the reactivity by acting as an electron reservoir. In this manner, the $[Fe_3S_4]$ subsite may act similarly to the $[Fe_4S_4]$ cluster components in the H- and A-clusters of [FeFe] hydrogenase and acetyl CoA synthase (ACS), respectively.[7,61,62]

## Spectroscopic investigations of NiFd provide a roadmap for characterization of the CODH electronic structure

Due to the high reactivity and complexity of native CODH, many steps within the catalytic mechanism for the reduction of $CO_2$ have not been well characterized.[7,16] With the development of nickel-substituted ferredoxin as a high-fidelity CODH model, it has become possible to gain detailed information on the simplified NiFd model in order to better understand the electronic structure of the C-cluster. The overall electronic configurations of $NiFd_{ox}$ and $NiFd_{red}$ are analogous to those of the CODH cubane subsite in $C_{ox}$ and $C_{red1}$, respectively, and $C_{red1}$, like $NiFd_{red}$, is the redox state of CODH that is known to bind both $CN^-$ and CO, albeit binding to both with weaker affinity than in CODH.[16,63] Further strengthening the utility of drawing a comparison between NiFd and the CODH C-cluster, we find that computationally, the electronic structure is dominated by the cubane core and fairly unresponsive to the distal protein contributions. Specifically, we found that the vertical spin ladder at the lowest-energy BS geometry was unaffected by either eliminating the electrostatic influence of the protein or

increasing the QM region. The insensitivity of the electronic structure to environmental embedding or including a better description of close-range polarization, which has been recently favored for understanding metalloenzyme electronic structure, indicates that the spin configuration is dominated by the first coordination sphere rather than electrostatic influences.[64] These computational studies allow the influence of the protein scaffold to be explored in a way otherwise inaccessible by experiment.

Previous Mössbauer spectroscopy studies on CODH have focused on the $C_{ox}$, $C_{red1}$, and CN-bound $C_{red1}$ clusters. In these studies, three unique iron sites were identified: FCII, which is now known to be the exogenous iron; FCIII, which is presumably one of the Fe centers in the heterometallic subsite; and a mixed-valent pair of iron sites.[15] The Mössbauer results from our studies highlight the distinct difference in the third iron site of $NiFd_{red}$. The isomer shift and quadrupole splitting of the $Fe_3$ site ($\delta = 0.50$ mm s$^{-1}$) of $NiFd_{red}$ is notably lower than FCIII ($\delta = 0.63$ mm s$^{-1}$) suggesting more electron density is localized onto that FCIII center in CODH.[15] This is likely best explained by considering the geometric structure, where the broken Ni-$S_{bridge}$ bond in CODH would disrupt the exchange pathway and localize more electron density on FCIII. These observed differences in Mössbauer parameters imply that the FCIII site may be one of the Fe centers located next to the open cubane sulfide. Moreover, the decrease of ~0.3 mm s$^{-1}$ observed for the quadrupole splitting of FCII when $CN^-$ binds to the Ni center in CODH is comparable to the changes at Fe that result from $CN^-$ binding to the nickel center in $NiFd_{red}$.[15] That the effects of ligand binding to the Ni center propagate to the Fe centers highlights the cooperative nature of all metal centers in the cluster.

In particular, analysis of the CO-bound NiFd species provides a unique opportunity to understand the largely uncharacterized, substrate-bound state of CODH. Historically, there has been controversy over the electronic structures of numerous CODH intermediates, with many proposed configurations for the $C_{red2}$ species. Amongst these, a biologically unprecedented formal $Ni^0$ species along with nickel-hydride species have been proposed.[16,65] Most recently, it has been postulated that the 2 additional electrons in the $C_{red2}$ state are located within the $CO_2$ adduct, and thus the $C_{red2}$ state cannot form in the absence of $CO_2$.[66] Model systems, such as NiFd and synthetic clusters, aid in the assignment of ambiguous electronic states of intermediates. In our system, the experimental data suggests that the NiFd–CO species is best modeled as an isolated $Ni^+$ center weakly interacting with the $[Fe_3S_4]^0$ cluster, which seems to act solely as an electron reservoir or buffer (Fig. 8). This may indicate that the $[NiFe_3S_4]$ heterometallic subsite may behave similarly upon CO binding. In this case, the C-cluster may be described as a binuclear $[NiFe_u]$ subsite that serves as the substrate binding site, which is coupled to an $[Fe_3S_4]$ subsite that modulates the electron density at the [NiFe] site. This arrangement would thus be similar to the structures of other enzyme active sites.[7,67] Additionally, this may explain the superior selectivity observed in CODH for $CO_2$ reduction over $H_2$ evolution, as the $[Fe_3S_4]$ subsite may buffer electron density to prevent formation of a deleterious nickel-hydride state, which could evolve $H_2$. Such intermediates are suspected in synthetic mononuclear $CO_2$ reduction catalysts, which exhibit nonselective reactivity potentially because they lack the ability to buffer electron density away from the active metal centers.[68–70] Experiments such as the ones carried out here, particularly the K-edge HERFD-XAS and variable-temperature, variable-field EPR spectroscopy, could provide detailed insight into the Ni site(s) in CODH.

## Conclusions

The nickel-substituted ferredoxin (NiFd) protein was probed in different redox- and ligand-bound states using a suite of advanced spectroscopic techniques to provide electronic information on the individual iron centers, the nickel site, and cluster altogether. Multifrequency EPR spectroscopy of the $NiFd_{red}$ and NiFd–CO species reveals full spin Hamiltonian parameters for the two clusters, including a unique spin-coupling scheme for NiFd–CO, while HERFD-XAS reveals element-specific insight into the electronic configuration of the nickel center, including spin state and structural distortion. The magnetic properties of the NiFd system provide insight into the electronic and geometric structures of the $C_{red1}$ and CO-bound states of CODH, proposing that the C-cluster may be explained more accurately as a [NiFe] subsite coupled to a $[Fe_3S_4]$ subsite to drive reactivity at the Ni center. The results from this work highlight the strength of utilizing multiple methods to connect the electronic structure of heterometallic iron–sulfur clusters with the complex, multielectron chemical transformations that they perform.

## Materials and methods

### Protein expression and purification

Pure samples of WT Pf Fd were obtained as described previously.[23,25] The plasmid (pTrc99aPfFd) containing the gene for fdxA for WT Pf Fd was received as a gift from Professor Michael Adams (University of Georgia). The plasmid was transformed into chemically competent JM105 *E. coli* cells (ATCC 47016). A 300 mL culture of Luria–Broth (LB) media containing 70 μg mL$^{-1}$ of carbenicillin (Gold-Bio) was grown at 37 °C while shaking at 200 rpm for 17 h. 50 mL of this culture was then used to inoculate 2 L of LB media supplemented with 70 μg mL$^{-1}$ carbenicillin and 25 μM FeCl3 (Ward's Science) in a 6 L flask. The culture was grown to $OD_{600}$ = 0.4 at 30 °C shaking at 200 rpm, at which point it was supplemented with 250 μM L-cysteine (BioBasic Canada). At $OD_{600}$ = 1.0 the cell cultures were then placed in a 4 °C bath to cool down prior to inducing protein expression by addition of 1 mM IPTG (Gold-Bio) at 30 °C shaking at 200 rpm for 12 h. The cells were harvested by centrifugation at 6800×*g* for 7 min at 4 °C. Finally, the cells were washed with 50 mM Tris-HCl buffer (VWR) and stored at −80 °C until lysis. To lyse the cells, the cell pellet was resuspended in 3 mL g$^{-1}$ cell pellet of 10 mM Tris-HCl buffer, pH 8.0, containing 100 mM NaCl (Fisher), 1 mM EDTA (VWR), 5 mM PMSF (GoldBio), and 0.33 mg mL$^{-1}$ of lysozyme (GoldBio). The

suspension was then incubated at 30 °C shaking at 200 rpm for 1 h, then the suspension was sonicated to further lyse the cells. Next, 50 μg $mL^{-1}$ of DNAse I (Gold-Bio) was added to the lysed cells, and the suspension was incubated for an additional 30 min at 30 °C shaking at 100 rpm. To precipitate additional *E. coli* proteins from the lysis solution, the suspension was heated to 65 °C for 1 h. Cellular debris was then pelleted out by centrifugation at 39 000×*g* for 30 min at 4 °C. The resulting clarified lysate was buffer-exchanged into 50 mM Tris–HCl buffer, pH 8.0, and loaded onto a HiTrapTM Q FF (Cytiva) anion exchange column. The protein was eluted using a 100 mL linear gradient from 0 to 0.6 M NaCl in Tris-HCl pH 8.0. Fractions containing Pf Fd WT were pooled together and dialyzed overnight into 5 mM sodium acetate, pH 3.0. Any resulting precipitate was pelleted out by centrifugation at 39 000×*g* for 10 min at 4 °C. The lysate was then loaded onto a HiTrapTM SP HP (Cytiva) cation exchange column in 5 mM sodium acetate buffer, pH 3.0. The protein was eluted using a 100 mL linear gradient from 0 to 0.6 M NaCl. Fractions containing Pf Fd were collected and exchanged into 50 mM Tris-HCl buffer, pH 8.0. This solution was concentrated and loaded onto a Sephadex G-75 size exclusion column (hand-packed) and eluted using 50 mM Tris-HCl buffer, pH 8.0. Pure fractions were collected and concentrated, before treatment with 50 mM $K_3Fe(CN)_6$ (Sigma) and 10 mM EDTA at RT for 2 h. The protein solution containing $[Fe_3S_4]^+$ Fd was then desalted using a 10-DG Desalting Column (Bio-Rad) to remove excess iron and ferricyanide and then concentrated and stored at 4 °C. Protein purity was verified using SDS-PAGE.

### Preparation of $^{57}FeSO_4$

The $^{57}FeSO_4$ solution was prepared by dissolving isotopically enriched $^{57}Fe$ (96.18%) metal (Cambridge Isotope Labs) with 2 molar equivalents of $H_2SO_4$ at 37 °C at 200 rpm for 12 h. After total dissolution, the solution was stored at −80 °C until ready to use.

### Minimal media growth using $^{57}FeSO_4$

Pure samples of $^{57}Fe$-labelled WT Pf Fd were obtained by heterologous expression of Pf Fd in JM105 *E. coli* cells in minimal media supplemented with $^{57}FeSO_4$. A 100 mL overnight starter culture of Luria-Broth media containing 70 μg $mL^{-1}$ of carbenicillin (GoldBio) was grown overnight at 37 °C while shaking at 200 rpm for 17 h. Then, 5 mL of this culture was used to inoculate 1 L of minimal media containing M9 salts, supplemented with 70 μg $mL^{-1}$ carbenicillin, 25 μM $^{57}FeSO_4$, 20 mM glucose (Fischer), 100 μM $CaCl_2$ (BioBasic), 2 mM $MgSO_4$ (BioBasic), and 100 μg $mL^{-1}$ thiamine (Sigma). The cells were incubated at 37 °C while shaking at 200 rpm until the optical density at 600 nm reached 0.3, at which point the culture was supplemented with 300 μM L-cysteine (BioBasic) and an additional 25 μM $^{57}FeSO_4$. The cells were continuously incubated at 37 °C while shaking at 200 rpm until an optical density at 600 nm reached 0.6, at which point the cells were placed into an ice bath for 15 min. Protein expression was induced using 1 mM IPTG (GoldBio), and the cells were allowed to incubate at 30 °C while shaking at 175 rpm for 16 h. The cells were harvested, lysed, and the protein purified as described previously.[23]

### Reconstitution of $[MFe_3S_4]$ (M = Ni) cluster in WT Pf Fd

Preparation of $[MFe_3S_4]^+$ Fd samples was performed as described previously.[123] To prepare $[MFe_3S_4]^+$ Fd samples, the purified $[Fe_3S_4]^+$ was reduced with 3 molar equivalents of sodium dithionite (DT, Beantown Chemical) for 20 min under an anaerobic atmosphere. After the cluster had been fully reduced, 20 molar equivalents of $Ni(NO_3)_2$ (Sigma-Aldrich) was added and allowed to incubate for 2 h under an anaerobic atmosphere. The resulting protein solution was then desalted using a 10-DG Desalting Column to remove excess metals and dithionite. To prepare $^{57}Fe$-labelled protein, the samples were prepared with the procedure listed above except that $[^{57}Fe_3S_4]$ Fd was used.

### Preparation of samples for CN binding studies with NiFd

All NiFd-CN samples were prepared in an anaerobic chamber ($O_2$ < 2 ppm) in 50 mM Tris buffer, pH 8. $NiFd_{red}$ aliquots at 50 μM and 250 μM were prepared based on $A_{408}$ for the Fe–S absorption band. Stock solutions of KCN were prepared in 50 mM Tris buffer, pH 8. A total of four samples were prepared at each protein concentration with 0.5, 1.0, 2.0 and 10.0 equivalents of KCN relative to protein. After addition of KCN, samples were allowed to sit for 20 minutes, then transferred to quartz EPR (X-band) tubes and flash frozen using $lN_2$. The fraction of NiFd-CN and $NiFd_{red}$ present at varying $CN^-$ concentrations was determined based on EPR spectral simulations. An approximate $K_D$ was calculated by fitting the data sets at 50 μM and 250 μM $NiFd_{red}$ to the Langmuir binding equation based on a one-site binding model (Fig. S23).

### Optimization of NiFd–CO sample preparation

CO binding to $NiFd_{red}$ is weak and the solubility of CO in aqueous solutions is low, so it was crucial to determine the optimal preparation conditions to maximize CO binding. For all samples, freshly reconstituted NiFd samples were incubated with 4 molar equivalents of DT in an anaerobic chamber. CO was then introduced to the headspace of a sealed borosilicate vial to 1 atm of CO at RT, 1 atm of CO while the vial was kept on ice, 2.7 atm of CO at RT, or 1 atm of CO while bubbling the solution with CO at RT. The samples were then allowed to incubate for 20 min under the CO atmosphere and 50–200 μL of the solution were directly loaded into EPR tubes and frozen in liquid nitrogen. Each preparation was from a different purification and nickel reconstitution of NiFd at concentrations ranging from 100 μM to 1 mM. For visualization, the spectra were normalized to the NiFd signal at $g = 5.6$. It was found that pressurization of the headspace with CO to 2.7 atm achieved the highest and most reproducible binding of CO (Fig. S24).

### Preparation of Mössbauer samples

All Mössbauer samples were prepared inside an anaerobic chamber ($O_2$ < 2 ppm) before 500 μL of solution was loaded into

a Delrin Mössbauer cup and frozen in $LN_2$. To confirm the purity of all samples, a small amount was loaded into a EPR tube (Wilmad Lab-Glass) and checked using CW-EPR spectroscopy (Fig. S22). All samples were prepared using $^{57}$Fe-labelled $[Fe_3S_4]$ Fd *in vivo*. To prepare the $[Fe_3S_4]^+$ Fd sample, 500 μL of 1 mM purified and freshly desalted protein was buffer exchanged into 50 mM CHES buffer (GoldBio), pH 8.5, and loaded into the Mössbauer cup. The $[Fe_3S_4]^0$ Fd sample was prepared by buffer exchanging 500 μL of 1 mM $[Fe_3S_4]^+$ Fd into 50 mM CHES buffer, pH 8.5, before incubating with 4 molar equivalents of DT for 20 min. The $NiFd_{red}$ sample was prepared by incubating 1 mM of freshly reconstituted and desalted $[NiFe_3S_4]$ Fd with 4 molar equivalents of DT in 50 mM CHES buffer, pH 8.5. After 10 min, 500 μL of the solution was loaded into a Mössbauer cup. The $NiFd_{ox}$ sample was prepared by incubating freshly reconstituted and desalted $[NiFeS_4]$ Fd with 20 molar equivalents of acetate (VWR) for 10 min in 50 mM CHES buffer, pH 8.5, and loaded into a Mössbauer cup. The NiFd-CN sample was prepared by incubating 1 mM of freshly reconstituted and desalted $[NiFe_3S_4]$ Fd with 4 molar equivalents of DT and 30 molar equivalents of KCN in 50 mM CHES buffer, pH 8.5. After 10 min, 500 μL of the solution was loaded into a Mössbauer cup. The NiFd–CO sample was prepared by incubating 1 mM of freshly reconstituted and desalted $[NiFe_3S_4]$ Fd with 10 molar equivalents of DT in 50 mM CHES buffer, pH 8.5. 600 μL of the solution was then loaded into a 2 mL borosilicate vial and sealed. The headspace was then evacuated and pressurized to 40 psi with CO. After 15 min, 500 μL of the solution was loaded into a Mössbauer cup. Caution! Cyanide samples must be handled at basic pHs (pH > 8) to avoid outgassing of toxic HCN fumes. All $CN^-$ and CO manipulation was carried out in a glovebox that was directly vented.

### Preparation of EPR samples

All EPR samples were prepared inside an anaerobic chamber ($O_2$ < 2 ppm) before loading into quartz EPR (X-band) tubes or FEP tubes (W-band). $^{57}$Fe-labelled samples of NiFd samples were prepared by using $^{57}$Fe-labelled $[Fe_3S_4]$ Fd prepared using the *in vivo* method. $NiFd_{red}$ was prepared by incubating 1 mM of freshly reconstituted and desalted $[NiFe_3S_4]$ Fd with 4 molar equivalents of DT in 100 mM CHES buffer, pH 8.0. After 10 min, the solution was diluted to 20% w/v glycerol before loading 62 μL of solution into an FEP tube, and 50 μL of solution into an EPR tube. NiFd–CO was prepared as described above, with 1 mM freshly reconstituted and desalted $[NiFe_3S_4]$ Fd.

### Preparation of XAS samples

Samples were prepared inside an anaerobic chamber ($O_2$ < 2 ppm) and checked for purity using EPR spectroscopy (Fig. S41). The $NiFd_{red}$, $NiFd_{ox}$ and NiFd-CN samples were prepared in 50 mM Tris buffer, pH 8, targeting a 1.5 mM protein concentration. The WT $[Fe_3S_4]^+$ Fd cluster was reconstituted with Ni by reducing WT $[Fe_3S_4]^+$ Fd with 6 equivalents of DT for 20 min with stirring. Then, 20 equivalents of $Ni(NO_3)_2$ were added to WT $[Fe_3S_4]^0$ Fd and allowed to stir for 2 hours. Protein solution was desalted using a 10-DG Desalting Column (Bio-Rad) equilibrated with 50 mM Tris buffer, pH 8, to obtain the as-isolated NiFd sample. Fractions containing NiFd were collected and concentrated using a 3 kDa Amicon® ultra centrifugal filter. For the $NiFd_{red}$ and NiFd-CN samples, 10 equivalents of DT were added to the concentrated protein solution and stirred for 20 minutes. For the NiFd-CN sample, 30 equivalents of KCN were added following DT addition, and the sample was stirred for an additional 20 minutes. For the $NiFd_{ox}$ sample, 20 equivalents of thionin acetate were added to the concentrated as-isolated NiFd protein solution and stirred for 20 minutes. Glycerol was added as a glassing agent to a final concentration of v/v 30% in each sample. Samples were then loaded into a white Delrin cylindrical cell (10 mm diameter × 10 mm height) with a Kapton tape-sealed window and frozen with liquid nitrogen. The NiFd–CO sample was prepped in 100 mM CHES buffer, pH 8, targeting a 1.5 mM protein concentration. After the addition of 6 equivalents of DT and 20 equivalents of $Ni(NO_3)_2$ to WT $[Fe_3S_4]^+$ Fd the protein solution was stirred for 2 hours under a CO headspace. Protein solution was then desalted with a 10-DG Desalting Column (Bio-Rad) equilibrated with CO-saturated 100 mM CHES buffer, pH 8. Protein fractions were concentrated using a 3 kDa Amicon® ultra centrifugal filter. Protein solution was transferred to a GC vial and placed on a chilled aluminum block, subsequently 10 equivalents of DT were added. CO was bubbled through protein solution *via* a needle for one hour and then pressurized with CO for 45 minutes. No glassing agent was added to NiFd–CO sample to prevent loss of bound CO. Sample was then transferred to a white Delrin cell with a Kapton tape-sealed window and frozen with liquid nitrogen.

### EPR spectroscopy

Continuous-wave (CW) X-band EPR spectra were collected using a Bruker EMXPlus equipped with a ColdEdge cryogen-free helium cryostat and recirculation system and an Oxford Instruments MercuryITC temperature controller. All presented spectra were obtained using a microwave frequency of 9.37 GHz and a modulation frequency and amplitude of 100 kHz and 10 G, respectively. Background signals were removed by baseline subtraction using IGOR Pro 9.00 (Wavemetrics, Lake Oswego, OR).

W-band electron spin echo-detected (ESE) field swept spectra were measured using the pulse sequence $t_p$–$\tau$–$2t_p$–$\tau$–echo. The length of the $\pi/2$ microwave pulse was set to $t_p = 32$ ns, and the interpulse delay was $\tau = 260$ ns for $NiFd_{red}$/NiFd–CO. The shot repetition time (SRT) was 500 μs. W-band $T_2$ relaxation experiments were collected using the pulse sequence $t_p$–$\tau_{vary}$ –$2t_p$–$\tau_{vary}$–echo, where $\tau_{vary}$ was in incremented from 250 ns–5 μs in logscale for a total of 201 pts. The echo intensities for each measurement are then plotted *vs.* time to give the decay traces. W-band $T_1$ inversion recovery experiments were collected using the pulse sequence $mw_{sat}$–$T$–$t_{wait}$–$t_p$–$\tau$–$2t_p$–$\tau$–echo with $mw_{sat}$ = 12 μs, and $T = 25$ μs and $t_{wait}$ incremented from 2 ns–3 ms for 501 pts. Nutation experiments were conducted using the pulse sequence $t_{prep}$–$\tau$–$t_{wait}$–$t_p$–$\tau$–$2t_p$–$\tau$–echo with $t_{prep}$ incremented from 2 ns to 800 ns with 201 points. Nutation frequencies were

determine by baseline correction of the time domain data, applying a Hamming window, and zero filling to 402 pts before applying a fast Fourier Transform (FFT) All spectra were simulated using the Easyspin plugin (version 5.23) Matlab toolbox.[71]

### Mössbauer spectroscopy

Variable temperature, variable field Mössbauer spectra were recorded using Janis Research Super-Varitemp dewars that allowed studies in parallel applied magnetic fields up to 7.0 T. Data were collected over the temperature range of 4.2–150 K. Mössbauer spectral simulations were performed using the WMOSS software package (SEE Co). Isomer shifts are quoted relative to Fe metal at 298 K.

### Ni Kα high energy resolution fluorescence detected X-ray absorption spectroscopy

Ni Kα HERFD-XAS spectra of all samples were collected at the Cornell High Energy Synchrotron Source (CHESS) ID2A: Photon-In Photon-Out X-ray Spectroscopy (PIPOXS) beamline. Samples were maintained at 80 K for the duration of experiments using a $lN_2$ cryostat from Lake Shore Cryotronics, Inc. A set of five Ni analyzer Si(620) crystals with 850 mm radius of curvature were used for light monochromatization and a Pilatus 100 K detector was used to collect the Ni Kα fluorescence data. The incident energy was calibrated to the first inflection point of a Ni metal foil (8333 eV). To ensure against photodamage, an appropriate beam flux was determined independently for each sample by evaluating photoreduction after subsequent scans and attenuating the beam until sequential scans gave overlapping spectra (Fig. S35–S38). Data were collected in the energy range 8200–8800 eV: 8200–8320 eV at 5 eV steps, 8320–8370 eV at 0.2 eV steps, 8370–8500 eV at 1.0 eV steps and 8500–8800 eV at 5 eV steps. Multiple scans were collected at fresh sample spots and averaged to give the final presented data. Spectra were processed using the Athena software package and normalized to a total intensity of 1 at the tailing plateau of the spectrum.[72] Edge positions were considered to be the energy at which the normalized intensity is at a value of 0.5.

### Computational model preparation and equilibration

$NiFd_{ox}$, $NiFd_{red}$, and NiFd–CO models were built using the X-ray crystal structure of the D14C $Fe_4S_4$ ferredoxin protein (PDB ID: 2Z8Q). The ChimeraX program was used to make the Fe → Ni substitution, the Cys14 → Asp14 substitution, as well as place the CO ligand for NiFd–CO.[73] Small model (the 1st coordination sphere) BS-DFT calculations using TURBOMOLE were used to generate metal force constants through the MCPB.py program, utilizing B3LYP-D3 and def2-TZVP basis set for all atoms, and charge fitting was performed similarly using a larger model to obtain a force field for the cluster.[74,75] The systems were solvated in a 10 Å water box described by the OPC water model, and all amino acids not bound to the cluster were parametrized using the ff19SB force field.[76,77] The AMBER22 program was used to equilibrate the structures using classical molecular dynamics (MD), using the following steps in order: solvent-only minimization, full system minimization, 100 ps heating to 310 K in NVT, 1 ns restrained NPT simulation to obtain constant density, 5 ns unrestrained NPT equilibration, and a 100 ns NPT production.[78] From 5 independent 100 ns simulations, the frame with the lowest average root-mean-squared deviation (RMSD) of the backbone was used to obtain representative structures for QM/MM.

### QM/MM analysis of spin states, Mössbauer and EPR parameters, and K-edge spectra

Single representative structures for $NiFd_{ox}$, $NiFd_{red}$, and NiFd–CO were chosen, as mentioned previously, for electronic structure analysis *via* mixed quantum mechanics-classical mechanics (QM/MM) simulations. The Chemshell package was used as the QM/MM driver, with ORCA 6.0.1 used for QM energies/gradients and analysis, and DL-POLY for the MM energies/gradients.[79–82] The QM region consists of the $NiFe_3S_4$ site and the primary sphere coordinating residues and ligands, and the rest of the systems were described by the classical force field used in MD. The ZORA-TPSSh functional, with a ZORA relativistic recontracted def2-TZVP basis set, was used for all atoms with D3 dispersion correction, which has been shown to provide reliable geometries at the QM and QM/MM level for Fe–S clusters.[83] The resolution of identity approximation with chain-of-spheres exchange (RIJCOSX) was utilized to accelerate the calculations.[84,85] For each structure, broken symmetry states were constructed using a converged high-spin (all metal sites ferromagnetically coupled) reference, and pairs of Ni and Fe were chosen to construct 3 broken symmetry states for each $NiFd_{ox/red/-CO}$, flipped after orbital localization built into ORCA. The choice of flipping $Fe_1$, $Fe_2$, or $Fe_3$ along with Ni (as labeled in Fig. 8A) corresponds to BS1, BS2, and BS3, respectively. The geometries of these representative structures were optimized using the broken-symmetry references, and the lowest energy geometries (BS3 for $NiFd_{red}$ and $NiFd_{ox}$, BS1 for NiFd–CO) were used for further analysis.

Natural population analysis (NPA) of the charges in the active site were computed *via* the Janpa program at the lowest energy geometries.[86] The other ground-state broken-symmetry densities, as well as the ferromagnetically coupled high-spin (HS) states, were computed at the geometries with the same level of theory as the optimization. A QM/MM calculation with a larger QM region was performed on the $NiFd_{red}$ system including residues Ile12, Gly13, Ala15, Ile16, Pro57, Val58, and three nearby water molecules in addition to the previously mentioned QM region, described by the same level of theory.

For $NiFd_{ox}$ state, Heisenberg exchange ($J$) couplings were computed between the Ni and Fe centers using the following phenomenological Hamiltonian:

$$\hat{H} = \widehat{H_0} + \sum_{i,j} J_{ij} \left\langle \widehat{S}_i \cdot \widehat{S}_j \right\rangle \quad (1)$$

which for collinear spins simplifies the total energy:

$$E = E_0 + \sum_{i,j} J_{ij} \left( S_{z,i} \cdot S_{z,j} \right) \quad (2)$$

where $S_{z,i}$ is the local spin on any Ni and Fe center, and $E_0$ is a constant factor to fit the Heisenberg exchange Hamiltonian.

The number of possible spin configurations exceeds the number of exchange $J$ terms, so they were solved for *via* singular value decomposition of eqn (2).[87]

Single-point calculations on the lowest energy geometries of $NiFd_{ox}$, $NiFd_{red}$, and NiFd–CO were used to compute Mössbauer and EPR parameters. The EPRNMR module of Orca was used to compute the $^{57}Fe$ parameters and hyperfine couplings.[88–90] The isomer shift $\delta$ was obtained from the computed charge density $\rho(0)$, following the benchmark provided in a previous study to match the level of theory used here.[91] To calculate the pre-edge transitions in the K-edge XAS spectra, TD-DFT was applied to the lowest energy geometries of $NiFd_{ox}$, $NiFd_{red}$, and NiFd–CO. Since this property concerns core electrons, the core properties basis set CP(PPP) was used to accurately model the excitations, and 50 roots were computed using the lowest energy orbital, corresponding to 1s on Ni.[54]

## Author contributions

Collection of EPR spectra and sample preparation for EPR and Mössbauer spectroscopy was done by LCL and HSS. Analysis of EPR spectra was performed by LCL and HSS. Mössbauer spectra were collected and analyzed by PB and KKM. HERFD-XAS experiments were designed, samples were prepared, and spectra collected by IPV and YL. HERFD-XAS data analysis was performed by IPV and HSS. Computational analysis was performed by PA. The manuscript was written by LCL, PB, PA, IV, YL, KM, ANA, and HSS. HSS was responsible for oversight and management of the project. All authors have given approval of the final version of the manuscript.

## Conflicts of interest

There are no conflicts to declare.

## Data availability

The data supporting this article have been included as part of the supplementary information (SI). Supplementary information: additional EPR and Mössbauer spectra and analysis, full XAS spectra, Tables S1–S6 including DFT-generated values, supplemental references. See DOI: https://doi.org/10.1039/d6sc00023a.

## Acknowledgements

This work was supported by the Department of Energy, Basic Energy Sciences, Physical Biosciences program (DE-SC0024869). Computational work was supported by NSF ACCESS grant CHE160054 for compute, and NIH-NIGMS grant R01GM134047. The Pf Fd plasmid (pTrc99aPfFd) was a generous gift from Professor Michael Adams (U. Georgia). LCL would like to acknowledge partial support from the Ohio State University and Lubrizol Foundation Fellowship. The authors would like to acknowledge Dr Justin North for his help in preparation of high-pressure gaseous samples, Manoj Subramanya, Thierry Dubroca, and Dr Stephen Hill for their assistance in W-band EPR data collection on the HiPER magnet at the National High Field Magnet Laboratory (NHFML) in Tallahassee, Florida. We would also like to thank Dr Yisong Guo and Jin Xiong for assistance in Mössbauer data collection at Carnegie Mellon University. A portion of this work was performed at the National High Magnetic Field Laboratory, which is supported by National Science Foundation Cooperative Agreement No. DMR-2128556, the State of Florida and U.S. Department of Energy. We would like to acknowledge Aadhishre Kasat and Cassie Huang for assistance with HERFD-XAS data collection. The authors would also like to acknowledge Dr Chris Pollock for assistance with the HERFD-XAS measurements. Part of this manuscript is based on research conducted at the Center for High-Energy X-ray Sciences (CHEXS), which is supported by the National Science Foundation (BIO, ENG and MPS Directorates) under award DMR-2342336. Molecular graphics and analyses were performed with UCSF ChimeraX, developed by the Resource for Biocomputing, Visualization, and Informatics at the University of California, San Francisco, with support from National Institutes of Health R01-GM129325 and the Office of Cyber Infrastructure and Computational Biology, National Institute of Allergy and Infectious Diseases.

## References

1 H. Beinert, R. H. Holm and E. Münck, Iron-Sulfur Clusters: Nature's Modular, Multipurpose Structures, *Science*, 1997, **277**(5326), 653–659, DOI: 10.1126/science.277.5326.653.
2 R. Cammack, *Iron–Sulfur Proteins in Encyclopedia of Biological Chemistry*, ed/ Lennarz, W. J. and Lane, M. D., Academic Press, Waltham, 2nd edn, 2013; pp pp 657–664, DOI: 10.1016/B978-0-12-378630-2.00222-X.
3 W. E. Broderick, B. M. Hoffman and J. B. Broderick, Mechanism of Radical Initiation in the Radical *S* -Adenosyl- l -Methionine Superfamily, *Acc. Chem. Res.*, 2018, **51**(11), 2611–2619, DOI: 10.1021/acs.accounts.8b00356.
4 D. C. Johnson, D. R. Dean, A. D. Smith and M. K. Johnson, Structure, Function, and Formation of Biological Iron-Sulfur Clusters, *Annu. Rev. Biochem.*, 2005, **74**(1), 247–281, DOI: 10.1146/annurev.biochem.74.082803.133518.
5 W. E. Broderick and J. B. Broderick, Radical SAM Enzymes: Surprises along the Path to Understanding Mechanism, *J. Biol. Inorg. Chem.*, 2019, **24**(6), 769–776, DOI: 10.1007/s00775-019-01706-w.
6 K. D. Karlin, Metalloenzymes, Structural Motifs, and Inorganic Models, *Science*, 1993, **261**(5122), 701–708, DOI: 10.1126/science.7688141.
7 M. Can, F. A. Armstrong and S. W. Ragsdale, Structure, Function, and Mechanism of the Nickel Metalloenzymes, CO Dehydrogenase, and Acetyl-CoA Synthase, *Chem. Rev.*, 2014, **114**(8), 4149–4174, DOI: 10.1021/cr400461p.
8 O. Einsle and D. C. Rees, Structural Enzymology of Nitrogenase Enzymes, *Chem. Rev.*, 2020, **120**(12), 4969–5004, DOI: 10.1021/acs.chemrev.0c00067.
9 C. C. Lee, Y. Hu and M. W. Ribbe, Unique Features of the Nitrogenase VFe Protein from *Azotobacter Vinelandii*, *Proc.*

 

*Natl. Acad. Sci. U.S.A.*, 2009, **106**(23), 9209–9214, DOI: 10.1073/pnas.0904408106.

10 J.-H. Jeoung and H. Dobbek, Carbon Dioxide Activation at the Ni,Fe-Cluster of Anaerobic Carbon Monoxide Dehydrogenase, *Science*, 2007, **318**(5855), 1461–1464, DOI: 10.1126/science.1148481.

11 V. Wang, S. W. Ragsdale and F. A. Armstrong, Investigations of the Efficient Electrocatalytic Interconversions of CO2 and CO by Nickel-Containing Carbon Monoxide Dehydrogenases, *Met. Ions Life Sci.*, 2014, **14**, 71–97, DOI: 10.1007/978-94-017-9269-1_4.

12 V. C.-C. Wang, S. W. Ragsdale and F. A. Armstrong, Investigations of Two Bidirectional Carbon Monoxide Dehydrogenases from Carboxydothermus Hydrogenoformans by Protein Film Electrochemistry, *ChemBioChem*, 2013, **14**(14), 1845–1851, DOI: 10.1002/cbic.201300270.

13 H. Dobbek, V. Svetlitchnyi, L. Gremer, R. Huber and O. Meyer, Crystal Structure of a Carbon Monoxide Dehydrogenase Reveals a [Ni-4Fe-5S] Cluster, *Science*, 2001, **293**(5533), 1281–1285, DOI: 10.1126/science.1061500.

14 J. Fesseler, J.-H. Jeoung and H. Dobbek, How the [$NiFe_4S_4$] Cluster of CO Dehydrogenase Activates $CO_2$ and $NCO^-$, *Angew. Chem., Int. Ed.*, 2015, **54**(29), 8560–8564, DOI: 10.1002/anie.201501778.

15 Z. Hu, N. J. Spangler, M. E. Anderson, J. Xia, P. W. Ludden, P. A. Lindahl and E. Münck, Nature of the C-Cluster in Ni-Containing Carbon Monoxide Dehydrogenases, *J. Am. Chem. Soc.*, 1996, **118**(4), 830–845, DOI: 10.1021/ja9528386.

16 P. A. Lindahl, The Ni-Containing Carbon Monoxide Dehydrogenase Family: Light at the End of the Tunnel?, *Biochemistry*, 2002, **41**(7), 2097–2105, DOI: 10.1021/bi015932+.

17 G. O. Tan, S. A. Ensign, S. Ciurli, M. J. Scott, B. Hedman, R. H. Holm, P. W. Ludden, Z. R. Korszun, P. J. Stephens and K. O. Hodgson, On the Structure of the Nickel/Iron/Sulfur Center of the Carbon Monoxide Dehydrogenase from Rhodospirillum Rubrum: An x-Ray Absorption Spectroscopy Study, *Proc. Natl. Acad. Sci. U.S.A.*, 1992, **89**(10), 4427–4431, DOI: 10.1073/pnas.89.10.4427.

18 D. Bonam, M. C. McKenna, P. J. Stephens and P. W. Ludden, Nickel-Deficient Carbon Monoxide Dehydrogenase from Rhodospirillum Rubrum: In Vivo and in Vitro Activation by Exogenous Nickel, *Proc. Natl. Acad. Sci. U. S. A.*, 1988, **85**(1), 31–35, DOI: 10.1073/pnas.85.1.31.

19 D. M. Fraser and P. A. Lindahl, Evidence for a Proposed Intermediate Redox State in the CO/CO2 Active Site of Acetyl-CoA Synthase (Carbon Monoxide Dehydrogenase) from Clostridium Thermoaceticum, *Biochemistry*, 1999, **38**(48), 15706–15711, DOI: 10.1021/bi990398f.

20 A. Majumdar, Bioinorganic Modeling Chemistry of Carbon Monoxide Dehydrogenases: Description of Model Complexes, Current Status and Possible Future Scopes, *Dalton Trans.*, 2014, **43**(32), 12135–12145, DOI: 10.1039/C4DT00729H.

21 M. S. Fataftah, D. W. N. Wilson, Z. Mathe, T. J. Gerard, B. Q. Mercado, S. DeBeer and P. L. Holland, Inserting Three-Coordinate Nickel into [4Fe-4S] Clusters, *ACS Cent. Sci.*, 2024, **10**(10), 1910–1919, DOI: 10.1021/acscentsci.4c00985.

22 D. W. N. Wilson, M. S. Fataftah, Z. Mathe, B. Q. Mercado, S. DeBeer and P. L. Holland, Three-Coordinate Nickel and Metal–Metal Interactions in a Heterometallic Iron–Sulfur Cluster, *J. Am. Chem. Soc.*, 2024, **146**(6), 4013–4025, DOI: 10.1021/jacs.3c12157.

23 L. C. Lewis and H. S. Shafaat, Reversible Electron Transfer and Substrate Binding Support [$NiFe_3S_4$] Ferredoxin as a Protein-Based Model for [NiFe] Carbon Monoxide Dehydrogenase, *Inorg. Chem.*, 2021, **60**(18), 13869–13875, DOI: 10.1021/acs.inorgchem.1c01323.

24 R. C. Conover, J. B. Park, M. W. W. Adams and M. K. Johnson, Formation and Properties of an Iron-Nickel Sulfide (NiFe3S4) Cluster in Pyrococcus Furiosus Ferredoxin, *J. Am. Chem. Soc.*, 1990, **112**(11), 4562–4564, DOI: 10.1021/ja00167a074.

25 L. C. Lewis, Electronic Isomerism in a Heterometallic Nickel–Iron–Sulfur Cluster Models Substrate Binding and Cyanide Inhibition of Carbon Monoxide Dehydrogenase, *Chem. Sci.*, 2024, **15**(16), 5916–5928, DOI: 10.1039/D4SC00023D.

26 S. Ciurli, P. K. Ross, M. J. Scott, S.-B. Yu and R. H. Holm, Synthetic Nickel-Containing Heterometal Cubane-Type Clusters with NiFe3Q4 Cores (Q = Sulfur, Selenium), *J. Am. Chem. Soc.*, 1992, **114**(13), 5415–5423, DOI: 10.1021/ja00039a063.

27 S. Ciurli, S. B. Yu, R. H. Holm, K. K. P. Srivastava and E. Munck, Synthetic Nickel-Iron NiFe3Q4 Cubane-Type Clusters (S = 3/2) by Reductive Rearrangement of Linear [Fe3Q4(SEt)4]3- (Q = Sulfur, Selenium), *J. Am. Chem. Soc.*, 1990, **112**(22), 8169–8171, DOI: 10.1021/ja00178a053.

28 R. Panda, Y. Zhang, C. C. McLauchlan, P. Venkateswara Rao, F. A. Tiago de Oliveira, E. Münck and R. H. Holm, Initial Structure Modification of Tetrahedral to Planar Nickel(II) in a Nickel−Iron−Sulfur Cluster Related to the C-Cluster of Carbon Monoxide Dehydrogenase, *J. Am. Chem. Soc.*, 2004, **126**(20), 6448–6459, DOI: 10.1021/ja030627s.

29 M.-E. Pandelia, N. D. Lanz, S. J. Booker and C. Krebs, Mössbauer Spectroscopy of Fe/S Proteins, *Biochim. Biophys. Acta Mol. Cell Res.*, 2015, **1853**(6), 1395–1405, DOI: 10.1016/j.bbamcr.2014.12.005.

30 W. R. Hagen, *EPR Spectroscopy of Iron—Sulfur Proteins. In Advances in Inorganic Chemistry*, Elsevier, 1992, Vol. 38, pp 165–222, DOI: 10.1016/S0898-8838(08)60064-1.

31 E. Muenck, P. G. Debrunner, J. C. M. Tsibris and I. C. Gunsalus, Moessbauer Parameters of Putidaredoxin and Its Selenium Analog, *Biochemistry*, 1972, **11**(5), 855–863, DOI: 10.1021/bi00755a027.

32 V. Papaefthymiou, J. J. Girerd, I. Moura, J. J. G. Moura, E. Muenck and S. of D. Moessbauer, Gigas Ferredoxin II and Spin-Coupling Model for Fe3S4 Cluster with Valence Delocalization, *J. Am. Chem. Soc.*, 1987, **109**(15), 4703–4710, DOI: 10.1021/ja00249a037.

33 K. K. P. Srivastava, K. K. Surerus, R. C. Conover, M. K. Johnson, J. B. Park, M. W. W. Adams and E. Munck,

Moessbauer Study of Zinc-Iron-Sulfur ZnFe3S4 and Nickel-Iron-Sulfur NiFe3S4 Clusters in Pyrococcus Furiosus Ferredoxin, *Inorg. Chem.*, 1993, **32**(6), 927–936, DOI: 10.1021/ic00058a029.

34 T. A. Kent, B. H. Huynh and E. Münck, Iron-Sulfur Proteins: Spin-Coupling Model for Three-Iron Clusters, *Proc. Natl. Acad. Sci. U. S. A.*, 1980, **77**(11), 6574–6576, DOI: 10.1073/pnas.77.11.6574.

35 M. I. Belinsky, The Spin-Coupling Model of Zero-Field Splitting for Trimeric [3Fe–4S] and Mixed-Metal [3FeZn–4S] Clusters of Ferredoxins from Pyrococcus Furiosus, *Chem. Phys.*, 2001, **263**(2), 279–300, DOI: 10.1016/S0301-0104(00)00361-X.

36 L. Noodleman, C. Y. Peng, D. A. Case and J.-M. Mouesca, Orbital Interactions, Electron Delocalization and Spin Coupling in Iron-Sulfur Clusters, *Coord. Chem. Rev.*, 1995, **144**, 199–244, DOI: 10.1016/0010-8545(95)07011-L.

37 W. Fu, J. Telser, B. M. Hoffman, E. T. Smith, M. W. W. Adams, M. G. Finnegan, R. C. Conover and M. K. Johnson, Interaction of Tl+ and Cs+ with the [Fe3S4] Cluster of Pyrococcus Furiosus Ferredoxin: Investigation by Resonance Raman, MCD, EPR, and ENDOR Spectroscopy, *J. Am. Chem. Soc.*, 1994, **116**(13), 5722–5729, DOI: 10.1021/ja00092a024.

38 R. C. Conover, A. T. Kowal, W. G. Fu, J. B. Park, S. Aono, M. W. Adams and M. K. Johnson, Spectroscopic Characterization of the Novel Iron-Sulfur Cluster in Pyrococcus Furiosus Ferredoxin, *J. Biol. Chem.*, 1990, **265**(15), 8533–8541, DOI: 10.1016/s0021-9258(19)38921-5.

39 R. E. Duderstadt, C. R. Staples, P. S. Brereton, M. W. W. Adams and M. K. Johnson, Effects of Mutations in Aspartate 14 on the Spectroscopic Properties of the [Fe3S4]+,0 Clusters in Pyrococcus Furiosus Ferredoxin, *Biochemistry*, 1999, **38**(32), 10585–10593, DOI: 10.1021/bi990670l.

40 B. H. Huynh, J. J. Moura, I. Moura, T. A. Kent, J. LeGall, A. V. Xavier and E. Münck, Evidence for a Three-Iron Center in a Ferredoxin from Desulfovibrio Gigas. Mössbauer and EPR Studies, *J. Biol. Chem.*, 1980, **255**(8), 3242–3244.

41 J. Telser, H.-I. Lee, E. T. Smith, H. Huang, P. Brereton, M. W. W. Adams, R. C. Conover, M. K. Johnson and B. M. Hoffman, Investigation by EPR and ENDOR Spectroscopy of the Novel 4Fe Ferredoxin from Pyrococcus Furiosus, *Appl. Magn. Reson.*, 1998, **14**(2–3), 305–321, DOI: 10.1007/BF03161897.

42 J. Telser, H. Huang, H.-I. Lee, M. W. W. Adams and B. M. Hoffman, Site Valencies and Spin Coupling in the 3Fe and 4Fe (S = 1/2) Clusters of Pyrococcus Furiosus Ferredoxin by 57Fe ENDOR, *J. Am. Chem. Soc.*, 1998, **120**(5), 861–870, DOI: 10.1021/ja971546x.

43 S. Stefan and D. Goldfarb, *EPR Spectroscopy: Fundamentals and Methods*, 2018.

44 E. C. Kisgeropoulos, Y. J. Gan, S. M. Greer, J. M. Hazel and H. S. Shafaat, Pulsed Multifrequency Electron Paramagnetic Resonance Spectroscopy Reveals Key Branch Points for One- vs Two-Electron Reactivity in Mn/Fe Proteins, *J. Am. Chem. Soc.*, 2022, **144**(27), 11991–12006, DOI: 10.1021/jacs.1c13738.

45 E. C. Kisgeropoulos, A. C. Manesis and H. S. Shafaat, Ligand Field Inversion as a Mechanism to Gate Bioorganometallic Reactivity: Investigating a Biochemical Model of Acetyl CoA Synthase Using Spectroscopy and Computation, *J. Am. Chem. Soc.*, 2021, **143**(2), 849–867, DOI: 10.1021/jacs.0c10135.

46 A. C. Brown and D. L. M. Suess, An Open-Cuboidal [Fe3S4] Cluster Characterized in Both Biologically Relevant Redox States, *J. Am. Chem. Soc.*, 2023, **145**(4), 2075–2080, DOI: 10.1021/jacs.2c13126.

47 A. K. Boudalis, Half-Integer Spin Triangles: Old Dogs, New Tricks, *Chem.–Eur. J.*, 2021, **27**(24), 7022–7042, DOI: 10.1002/chem.202004919.

48 P. A. S. Cruickshank, D. R. Bolton, D. A. Robertson, R. I. Hunter, R. J. Wylde and G. M. Smith, A Kilowatt Pulsed 94 GHz Electron Paramagnetic Resonance Spectrometer with High Concentration Sensitivity, High Instantaneous Bandwidth, and Low Dead Time, *Rev. Sci. Instrum.*, 2009, **80**(10), 103102, DOI: 10.1063/1.3239402.

49 M. V. H. Subramanya, J. Marbey, K. Kundu, J. E. McKay and S. Hill, Broadband Fourier-Transform-Detected EPR at W-Band, *Appl. Magn. Reson.*, 2023, **54**(1), 165–181, DOI: 10.1007/s00723-022-01499-3.

50 L. S. Kau, D. J. Spira-Solomon, J. E. Penner-Hahn, K. O. Hodgson and E. I. Solomon, X-Ray Absorption Edge Determination of the Oxidation State and Coordination Number of Copper. Application to the Type 3 Site in Rhus Vernicifera Laccase and Its Reaction with Oxygen, *J. Am. Chem. Soc.*, 1987, **109**(21), 6433–6442, DOI: 10.1021/ja00255a032.

51 A. C. Manesis, B. W. Musselman, B. C. Keegan, J. Shearer, N. Lehnert and H. S. Shafaat, A Biochemical Nickel(I) State Supports Nucleophilic Alkyl Addition: A Roadmap for Methyl Reactivity in Acetyl Coenzyme A Synthase, *Inorg. Chem.*, 2019, **58**(14), 8969–8982, DOI: 10.1021/acs.inorgchem.8b03546.

52 A. C. Manesis, A. Yerbulekova, J. Shearer and H. S. Shafaat, Thioester Synthesis by a Designed Nickel Enzyme Models Prebiotic Energy Conversion, *Proc. Natl. Acad. Sci. U.S.A.*, 2022, **119**(30), e2123022119, DOI: 10.1073/pnas.2123022119.

53 S. DeBeer George, T. Petrenko and F. Neese, Prediction of Iron K-Edge Absorption Spectra Using Time-Dependent Density Functional Theory, *J. Phys. Chem. A*, 2008, **112**(50), 12936–12943, DOI: 10.1021/jp803174m.

54 P. Chandrasekaran, S. C. E. Stieber, T. J. Collins, J. Lawrence Que, F. Neese and S. DeBeer, Prediction of High-Valent Iron K-Edge Absorption Spectra by Time-Dependent Density Functional Theory, *Dalton Trans.*, 2011, **40**(42), 11070–11079, DOI: 10.1039/C1DT11331C.

55 A. W. E. Dilg, G. Mincione, K. Achterhold, O. Iakovleva, M. Mentler, C. Luchinat, I. Bertini and F. G. Parak, Simultaneous Interpretation of Mössbauer, EPR and 57Fe ENDOR Spectra of the [Fe4S4] Cluster in the High-Potential Iron Protein I Ectothiorhodospira Halophila, *JBIC*, 1999, **4**(6), 727–741, DOI: 10.1007/s007750050345.

 

56 J. Meyer and J.-M. Moulis, Replacement of Sulfide by Selenide in the [4Fe-4S] Clusters of the Ferredoxin fromClostridium pasteurianumClostridium Pasteurianum, *Biochem. Biophys. Res. Commun.*, 1981, **103**(2), 667–673, DOI: 10.1016/0006-291X(81)90502-7.

57 E. Krahn, B. Weiss, M. Kröckel, J. Groppe, G. Henkel, S. Cramer, A. Trautwein, K. Schneider and A. Müller, The Fe-Only Nitrogenase from Rhodobacter Capsulatus: Identification of the Cofactor, an Unusual, High-Nuclearity Iron-Sulfur Cluster, by Fe K-Edge EXAFS and 57Fe Mössbauer Spectroscopy, *J. Biol. Inorg. Chem.*, 2002, **7**(1–2), 37–45, DOI: 10.1007/s007750100263.

58 J. B. Solomon, K. Tanifuji, C. C. Lee, A. J. Jasniewski, B. Hedman, K. O. Hodgson, Y. Hu and M. W. Ribbe, Characterization of a Nitrogenase Iron Protein Substituted with a Synthetic [Fe4Se4] Cluster, *Angew. Chem., Int. Ed.*, 2022, **61**(19), e202202271, DOI: 10.1002/anie.202202271.

59 A fast intrinsic localization procedure applicable for ab initio and semiempirical linear combination of atomic orbital wave functions | The Journal of Chemical Physics | AIP Publishing, https://pubs.aip.org/aip/jcp/article/90/9/4916/791853/A-fast-intrinsic-localization-procedure-applicable, accessed 2026-03-12.

60 T. M. Gilbert, π Acceptor Abilities of Anionic Ligands: Comparisons Involving Anionic Ligands Incorporated into Linear D10 [(NH3)Pd(A)]−, Square Planar D8 [(NN2)Ru(A)]−, and Octahedral D6 [(AsN4)Tc(A)]− Complexes, *Inorg. Chem.*, 2023, **62**(21), 8069–8079, DOI: 10.1021/acs.inorgchem.2c03778.

61 F. Wittkamp, M. Senger, S. T. Stripp and U.-P. Apfel, [FeFe]-Hydrogenases: Recent Developments and Future Perspectives, *Chem. Commun.*, 2018, **54**(47), 5934–5942, DOI: 10.1039/C8CC01275J.

62 H. S. Shafaat, A. C. Manesis and A. Yerbulekova, How to Build a Metalloenzyme: Lessons from a Protein-Based Model of Acetyl Coenzyme A Synthase, *Acc. Chem. Res.*, 2023, **56**(9), 984–993, DOI: 10.1021/acs.accounts.2c00824.

63 M. E. Anderson and P. A. Lindahl, Organization of Clusters and Internal Electron Pathways in CO Dehydrogenase from Clostridium Thermoaceticum: Relevance to the Mechanism of Catalysis and Cyanide Inhibition, *Biochemistry*, 1994, **33**(29), 8702–8711, DOI: 10.1021/bi00195a011.

64 S. Sumner, P. Söderhjelm and U. Ryde, Effect of Geometry Optimizations on QM-Cluster and QM/MM Studies of Reaction Energies in Proteins, *J. Chem. Theory Comput.*, 2013, **9**(9), 4205–4214, DOI: 10.1021/ct400339c.

65 P. Amara, J.-M. Mouesca, A. Volbeda and J. C. Fontecilla-Camps, Carbon Monoxide Dehydrogenase Reaction Mechanism: A Likely Case of Abnormal CO2 Insertion to a Ni−H− Bond, *Inorg. Chem.*, 2011, **50**(5), 1868–1878, DOI: 10.1021/ic102304m.

66 Y. Basak, C. Lorent, J.-H. Jeoung, I. Zebger and H. Dobbek, Metalloradical-Driven Enzymatic CO2 Reduction by a Dynamic Ni–Fe Cluster, *Nat. Catal.*, 2025, **8**(8), 794–803, DOI: 10.1038/s41929-025-01388-5.

67 P. S. Corrigan, S. H. Majer and A. Silakov, Evidence of Atypical Structural Flexibility of the Active Site Surrounding of an [FeFe] Hydrogenase from Clostridium Beijerinkii, *J. Am. Chem. Soc.*, 2023, **145**(20), 11033–11044, DOI: 10.1021/jacs.2c13458.

68 S. L. Behnke, A. C. Manesis and H. S. Shafaat, Spectroelectrochemical Investigations of Nickel Cyclam Indicate Different Reaction Mechanisms for Electrocatalytic $CO_2$ and $H^+$ Reduction, *Dalton Trans.*, 2018, **47**(42), 15206–15216, DOI: 10.1039/C8DT02873G.

69 R. Schneider, C. Lewis, S. Shafaat and H. The Good, the Neutral, and the Positive: Buffer Identity Impacts CO 2 Reduction Activity by Nickel( Ii ) Cyclam, *Dalton Trans.*, 2019, **48**(42), 15810–15821, DOI: 10.1039/C9DT03114F.

70 J. D. Froehlich and C. P. Kubiak, The Homogeneous Reduction of CO2 by [Ni(Cyclam)]+: Increased Catalytic Rates with the Addition of a CO Scavenger, *J. Am. Chem. Soc.*, 2015, **137**(10), 3565–3573, DOI: 10.1021/ja512575v.

71 S. Stoll and A. Schweiger, EasySpin, a Comprehensive Software Package for Spectral Simulation and Analysis in EPR, *J. Magn. Reson.*, 2006, **178**(1), 42–55, DOI: 10.1016/j.jmr.2005.08.013.

72 B. Ravel, M. Newville and H. E. P. H. Artemis, Data Analysis for X-Ray Absorption Spectroscopy Using *IFEFFIT*, *J Synchrotron Rad*, 2005, **12**(4), 537–541, DOI: 10.1107/S0909049505012719.

73 E. C. Meng, T. D. Goddard, E. F. Pettersen, G. S. Couch, Z. J. Pearson, J. H. Morris and T. E. Ferrin, UCSF ChimeraX: Tools for Structure Building and Analysis, *Protein Sci.*, 2023, **32**(11), e4792, DOI: 10.1002/pro.4792.

74 Y. J. Franzke, C. Holzer, J. H. Andersen, T. Begušić, F. Bruder, S. Coriani, F. Della Sala, E. Fabiano, D. A. Fedotov, S. Fürst, S. Gillhuber, R. Grotjahn, M. Kaupp, M. Kehry, M. Krstić, F. Mack, S. Majumdar, B. D. Nguyen, S. M. Parker, F. Pauly, A. Pausch, E. Perlt, G. S. Phun, A. Rajabi, D. Rappoport, B. Samal, T. Schrader, M. Sharma, E. Tapavicza, R. S. Treß, V. Voora, A. Wodyński, J. M. Yu, B. Zerulla, F. Furche, C. Hättig, M. Sierka, D. P. Tew and F. Weigend, TURBOMOLE: Today and Tomorrow, *J. Chem. Theory Comput.*, 2023, **19**(20), 6859–6890, DOI: 10.1021/acs.jctc.3c00347.

75 P. Li and K. M. Merz Jr, MCPB.Py: A Python Based Metal Center Parameter Builder, *J. Chem. Inf. Model.*, 2016, **56**(4), 599–604, DOI: 10.1021/acs.jcim.5b00674.

76 S. Izadi, R. Anandakrishnan and A. V. Onufriev, Building Water Models: A Different Approach, *J. Phys. Chem. Lett.*, 2014, **5**(21), 3863–3871, DOI: 10.1021/jz501780a.

77 C. Tian, K. Kasavajhala, K. A. A. Belfon, L. Raguette, H. Huang, A. N. Migues, J. Bickel, Y. Wang, J. Pincay, Q. Wu and C. Simmerling, ff19SB: Amino-Acid-Specific Protein Backbone Parameters Trained against Quantum Mechanics Energy Surfaces in Solution, *J. Chem. Theory Comput.*, 2020, **16**(1), 528–552, DOI: 10.1021/acs.jctc.9b00591.

78 D. A. Case, H. M. Aktulga, K. Belfon, I. Y. Ben-Shalom, J. T. Berryman, S. R. Brozell, F. S. Carvahol, D. S. Cerutti, T. E. Cheatham III, G. A. Cisneros, V. W. D. Cruzeiro,

T. A. Darden, N. Forouzesh, M. Ghazimirsaeed, G. Giambaşu, T. Giese, M. K. Gilson, H. Gohlke, A. W. Goetz, J. Harris, Z. Huang, S. Izadi, S. A. Izmailov, K. Kasavajhala, M. C. Kaymak, I. Kolossv\'a ry, A. Kovalenko, T. Kurtzman, T. S. Lee, P. Li, Z. Li, C. Lin, J. Liu, T. Luchko, R. Luo, M. Machado, M. Manathunga, K. M. Merz, Y. Miao, O. Mikhailovskii, G. Monard, H. Nguyen, K. A. O'Hearn, A. Onufriev, F. Pan, S. Pantano, A. Rahnamoun, D. R. Roe, A. Roitberg, C. Sagui, S. Schott-Verdugo, A. Shajan, J. Shen, C. L. Simmerling, N. R. Skrynnikov, J. Smith, J. Swails, R. C. Walker, J. Wang, J. Wang, X. Wu, Y. Wu, Y. Xiong, Y. Xue, D. M. York, C. Zhao, Q. Zhu, and P. A. Kollman. *Amber 2022; Univeristy Of California*, San Francisco, 2022.

79 J. Kästner, J. M. Carr, T. W. Keal, W. Thiel, A. Wander and P. D. L. Sherwood, An Open-Source Geometry Optimizer for Atomistic Simulations, *J. Phys. Chem. A*, 2009, **113**(43), 11856–11865, DOI: 10.1021/jp9028968.

80 F. Neese, The ORCA Program System, *WIREs Comput. Mol. Sci.*, 2012, **2**(1), 73–78, DOI: 10.1002/wcms.81.

81 F. Neese, Software Update: The ORCA Program System—Version 6.0, *WIREs Comput. Mol. Sci.*, 2025, **15**(2), e70019, DOI: 10.1002/wcms.70019.

82 M. F. Guest, A. M. Elena and A. B. G. Chalk, DL_POLY - A Performance Overview Analysing, Understanding and Exploiting Available HPC Technology, *Mol. Simul.*, 2021, **47**(2–3), 194–227, DOI: 10.1080/08927022.2019.1603380.

83 B. Benediktsson and R. Bjornsson, Analysis of the Geometric and Electronic Structure of Spin-Coupled Iron–Sulfur Dimers with Broken-Symmetry DFT: Implications for FeMoco, *J. Chem. Theory Comput.*, 2022, **18**(3), 1437–1457, DOI: 10.1021/acs.jctc.1c00753.

84 F. Neese, An Improvement of the Resolution of the Identity Approximation for the Formation of the Coulomb Matrix, *J. Comput. Chem.*, 2003, **24**(14), 1740–1747, DOI: 10.1002/jcc.10318.

85 F. Neese, F. Wennmohs, A. Hansen and U. Becker, Efficient, Approximate and Parallel Hartree–Fock and Hybrid DFT Calculations. A 'Chain-of-Spheres' Algorithm for the Hartree–Fock Exchange, *Chem. Phys.*, 2009, **356**(1), 98–109, DOI: 10.1016/j.chemphys.2008.10.036.

86 T. Y. Nikolaienko, L. A. Bulavin and D. M. Hovorun, JANPA: An Open Source Cross-Platform Implementation of the Natural Population Analysis on the Java Platform, *Comput. Theor. Chem.*, 2014, **1050**, 15–22, DOI: 10.1016/j.comptc.2014.10.002.

87 S. Zein, M. Poor Kalhor, L. F. Chibotaru and H. Chermette, Density Functional Estimations of Heisenberg Exchange Constants in Oligonuclear Magnetic Compounds: Assessment of Density Functional Theory versus Ab Initio, *J. Chem. Phys.*, 2009, **131**(22), 224316, DOI: 10.1063/1.3264570.

88 F. Neese, Prediction of Electron Paramagnetic Resonance g Values Using Coupled Perturbed Hartree–Fock and Kohn–Sham Theory, *J. Chem. Phys.*, 2001, **115**(24), 11080–11096, DOI: 10.1063/1.1419058.

89 F. Neese, Prediction and Interpretation of the 57Fe Isomer Shift in Mössbauer Spectra by Density Functional Theory, *Inorg. Chim. Acta*, 2002, **337**, 181–192, DOI: 10.1016/S0020-1693(02)01031-9.

90 F. Neese, Efficient and Accurate Approximations to the Molecular Spin-Orbit Coupling Operator and Their Use in Molecular g-Tensor Calculations, *J. Chem. Phys.*, 2005, **122**(3), 034107, DOI: 10.1063/1.1829047.

91 A. Banerjee, Q. Liu, J. Shanklin and M. Z. Ertem, Predicting Mössbauer Parameters of Nonheme Diiron Complexes with Density Functional Theory, *Inorg. Chem.*, 2023, **62**(29), 11402–11413, DOI: 10.1021/acs.inorgchem.3c00969.